R&D OF A HIGH-PERFORMANCE DIRC DETECTOR FOR USE IN AN ELECTRON-ION COLLIDER

by

S. Lee Allison
MS in Physics

A Dissertation Submitted to the Faculty of
Old Dominion University in Partial Fulfillment of the
Requirements for the Degree of

DOCTOR OF PHILOSOPHY

PHYSICS

OLD DOMINION UNIVERSITY
May 2017

Approved by:

Charles Hyde (Director)

Gagik Gavalian (Member)

Mark Havey (Member)

Grzegorz Kalicy (Member)

Jay Van Orden (Member)

Mike Overstreet (Member)

ABSTRACT

R&D OF A HIGH-PERFORMANCE DIRC DETECTOR FOR USE IN AN ELECTRON-ION COLLIDER

S. Lee Allison
Old Dominion University, 2017
Director: Dr. Charles Hyde

text of abstract goes here

ACKNOWLEDGEMENTS

Contents

LIST OF TABLES **vii**

LIST OF FIGURES **viii**

Chapter

1. INTRODUCTION **2**

2. ELECTRON-ION COLLIDER **3**
2.1 SCIENCE GOALS 4
2.2 FACILITIES 6

3. DIRC TECHNOLOGY **12**
3.1 CHERENKOV RADIATION 12
3.2 APPLYING THE CHERENKOV EFFECT TO PARTICLE ID 13
3.3 RING IMAGING DETECTORS 14
3.4 DIRC DETECTORS 14
3.5 HIT PATTERNS AND PARTICLE SEPARATION METHODS 19

4. HIGH-PERFORMANCE DIRC@EIC **28**
4.1 HIGH-PERFORMANCE DIRC COMPONENTS AND DESIGN 28
4.2 SIMULATED PERFORMANCE 31
4.3 POTENTIAL OPTIMIZATIONS 31

5. TESTING DIRC COMPONENTS **34**
5.1 OPTICAL PROPERTIES OF 3-LAYER LENS 34
5.2 RADIATION HARDNESS OF NLAK33 36
5.3 PERFORMANCE OF MCP-PMTS IN HIGH MAGNETIC FIELD 37

6. 3-LAYER LENS PERFORMANCE IN PARTICLE BEAM **43**
6.1 SIMULATED PERFORMANCE 43
6.2 2015 TEST BEAM PROTOTYPE SETUP 43
6.3 DATA ANALYSIS 43

7. OUTLOOK AND SUMMARY **44**

BIBLIOGRAPHY **44**

APPENDICES
A. ERROR EVALUATION 48

VITA **49**

List of Tables

List of Figures

2.1. The reduced cross section $\sigma_r(x, Q^2)$ as a function of Q^2. Filled circles are combined H1 and Zeus data from HERA for proton-positron collisions, hollow squares are from fixed target experiments, and the yellow is prediction from HERAPDF0.1. [1] 4
2.2. Evolution of our understanding of nucleon spin structure. Left: In the 1980s, a nucleons spin was naively explained by the alignment of the spins of its constituent quarks. Right: In the current picture, valence quarks, sea quarks and gluons, and their possible orbital motion are expected to contribute to overall nucleon spin. [2] 5
2.3. Top: Ratios of ^{3}He to Deuterium DIS cross sections from JLab (circles) and HERMES (triangles). Bottom: Ratios of ^{4}He to Deuterium DIS cross sections from JLab (circles), SLAC (squares), and HERMES (triangles) [3]. 8
2.4. Momentum distributions for pions (blue) and kaons (magenta) from the pythia simulation package for DIS events corresponding to collisions between 10 GeV electrons and 100 GeV protons, a common BNL/JLab kinematic, shown for a bin of $10 < Q2 < 100$ GeV^2. 9
2.5. Current design of the EIC facility for JLab with the two interaction points (IPs) highlighted in red (top), and the current baseline design for the detector at IP1 (bottom). 10
2.6. Current design of the EIC facility at BNL (top), and the proposed BeAST (Brookhaven eA Solenoidal Tracker) detector (bottom). 11
3.1. Illustration of the Cherenkov cone. 13
3.2. Particle momentum [GeV/c] versus Cherenkov angle [mrad] for different particle species in fused silica ($n \approx 1.473$). While the full range (left) makes it seem as if separation between heavier species becomes more and more challenging, zooming in (right) shows that it is indeed possible separate protons, kaons, and pions even at higher particle momentum. 14
3.3. Basic concept of a proximity focusing Ring Imaging Cherenkov (RICH) detector (a), and an example of how they can be used to do PID based on particle mass (b). 15
3.4. The basic components of a DIRC detector: a solid radiator, typically fused silica (green); a mirror to redirect backward-going photons (pink); optional focusing optics (purple); an expansion volume to allow photons to separate in space (cyan); and a detector surface to record the position and arrival time of Cherenkov photons (blue). 16
3.5. Schematic of BaBar DIRC and detection region. 17

3.6. Performance of the BaBar DIRC for $e^+e^- \to \mu^+\mu^-$ events. a) shows the difference between the measured and expected Cherenkov angle (dots) and a Gaussian fit to the data with a 2.5 mrad width (line). b) is the average number of detected photons vs. track polar angle for data (dots) and Geant4 [4] simulation (line). 18
3.7. Evolution of the DIRC concept. From top left to bottom right: BaBar Barrel DIRC, Focusing DIRC, PANDA Barrel DIRC, PANDA Disc DIRC, Belle II Time of Propagation DIRC, LHCb TORCH DIRC, GlueX DIRC, EIC DIRC 18
3.8. Various detector geometries (left) and the resulting simulated hit patterns (right) from 1000 identical particles. A typical RICH detector (a), produces a very nice ring pattern. A DIRC detector with a sufficiently large expansion volume using a thin radiator bar (b) produces two ring segments. A DIRC with a radially compact expansion volume (c) will reflect one of the ring segments so that it will stack side by side. Finally, a DIRC detector with a compact expansion volume both radially and transversely (i.e. into and out of the page) (d) will cause the ring segments to fold in on themselves, making a fish-like pattern. The DIRC patterns are viewed from the back of the detector plane and rotated 90° clockwise relative to the corresponding geometry. . . . 20
3.9. For a prism-shaped expansion volume (a) different segments of the hit pattern correspond to different paths taken (b). Paths with multiple reflections inside the prism (e.g. bottom-left) have been excluded for simplicity. 21
3.10. Schematic of the geometric reconstruction concept, with a photon (purple) being emitted from the particle track. The direction of the k-vector can be used to determine the original direction vector, $\vec{k}_{org}$, of the photon and is used for the reconstruction of θ_C. 22
3.11. 2D illustration showing all possible combinations of k-vector directions off of the particle track. Not shown are the additional 4 components where $k_x \to -k_x$. 23
3.12. 2D example of averaging LUT entries to reduce prism ambiguity reconstructions. The two photons reflecting off of the bottom prism face (blue) have been averaged to the one black photon. The two photons reflecting off of the top prism face (orange) have been average to the red photon. In this simplified example the number of entries in the lookup table have been reduced by half. Angles have been exaggerated. 24
3.13. Illustration of possible ambiguities in the θ_C reconstruction coming from possible paths in a prism-shaped expansion volume. Each face is labeled in a) along with an example of a direct path, while b) shows 3 possible paths that lead from the bar to a certain pixel: 1 top reflection (gold), 1 bottom reflection (blue), and 1 direct path (gray). 25

3.14. Simulated reconstructed Cherenkov angle per photon from a 7 GeV/c particle with a polar angle of 125° for: a) one photon from a proton with only bar ambiguities, b) all photons from one proton with only bar ambiguities, c) all photons from 1000 identical protons with only bar ambiguities, d) all photons from 1000 identical protons with both bar and prism ambiguities, e) same as d) but with constraints on the photon angle with the bar surface and neglecting y direction flips due to zero beam divergence, and f) a zoom showing a buildup around the calculated value of 816 mrad along with a combinatorial background. 26
3.15. Example time-based reconstruction for a plate radiator with a prism expansion volume for kaons (dashed) and pions (red). Photon arrival times for one MCP-PMT pixel are shown in a), and b) is the log-likelihood difference for kaon and pion hypotheses for a smaple of 3.5 GeV/c particles at 22° polar angle [5]. 27
4.1. Pion-kaon separation as a function of particle momentum for different assumptions of the per track Cherenkov angle resolution. The PID requirements of the EIC necessitate a per track resolution of 1 mrad, while BaBar and PANDA needed only 2.5 mrad resolution. 29
4.2. Left: full Geant4 simulation of the current DIRC at EIC baseline design with 16 bar boxes, 176 radiator bars, a 3-layer lens focusing optic, and a 38° prism expansion volume. Right: a zoom in on a single bar box and the layering of the lens. 30
4.3. Simulated hit pattern of PANDA DIRC without (black) and with (red) air gap lens focusing (a). On the outer edges of the ring image the lens is becoming dispersive and losing photons, while near the center of the rings the lens does a good job of focusing the image, as seen more clearly in b). 31
4.4. Comparison of the photon yield per track for a DIRC bar with no focusing (green), a standard air gap lens (red), and a 2-layer compound lens (blue) for polar angles of 125° (left) and 90° (right). The standard and compound lenses have comparable yields at 125°, but the standard lens clearly loses a large amount of photons in the perpendicular case. 32
4.5. The simulated focal planes (red lines) of a 2-layer lens (left) and the 3-layer lens (right) compared to the shape of the expansion volume prism (grey). Obviously the focal plane of the 2-layer lens is highly parabolic in shape, whereas the 3-layer lens focal plane is relatively flat, allowing for a better resolution of the Cherenkov angle. 32
4.6. Prototype 3-layer lens built for optical testing (a), and an exploded view of each layer with dimensions (b). 33
5.1. Schematic drawing of the setup built at Old Dominion University for testing the optical properties of the 3-layer lens design (left), and a closeup view of the lens and screen inside the actual setup (right). 34
5.2. CAD drawing of 3-layer lens holder which lets the lens rotate in two planes, allowing the full 3D focal plane to be mapped. 35
5.3. Initial measurement of the 3-layer lens focal plane using the upgraded green laser (red dots) compared to simulation (blue line). 36

5.4. Schematic of the discrepancy between beam positions in data (black) and simulation (yellow) in relation to the original beam positions (blue) for a given rotation point (red) at the center (top) of the lens, or at the edge (bottom) of the lens. 37
5.5. Initial measurement of the 3-layer lens focal plane compared to a rotation corrected simulation (a), and a second measurement with a tighter (2 mm) beam configuration and a modified lens holder (b). 39
5.6. X-ray source (a) and monochromator (b) used for testing the radiation hardness through transmission degradation of NLaK33 samples at Catholic University of America. 40
5.7. Schematic of the Micro-channel Plate photo-multiplier tube (MCP-PMT) concept. A cathode and anode sandwich two conducting plates with micrometer-sized channels (MCP) in a chevron pattern. An incident photon (blue) strikes the cathode, producing a photo-electron (red). That electron is accelerated through the potential difference between the cathode and first MCP (HV1) before striking the inside of one channel. This creates the same effect as an electron striking the dynode of a typical PMT, resulting in an avalanche of photo-electrons that emerge out of the other side of the first MCP. These electrons are again accelerated through a second potential difference (HV2) before repeating the process in the second MCP. Finally, the copious photo-electrons exit the second MCP, are accelerated through a final potential difference (HV3), and are collected on the anode. This design is both much more compact and much more resistant to magnetic fields compared to traditional PMTs. 41
5.8. The FROST superconducting magnet with the dark box placed in the bore. . 42
5.9. Left: A closeup of the dark box showing the Photek PMT210 being held in place by the turn table. This setup allows the MCP-PMT to be rotated around both the horizontal Z(Z') axis as well as the vertical Y(Y') axis (with respect to the floor). The rotation about the Y(Y') and Z(Z') axes are described by the polar angle θ and azimuthal angle ϕ respectively. The magnetic field is parallel to the central axis of the dark box. Right: A flowchart of the readout used for testing. The photocathode is exposed to single 470 nm photons to produce photoelectrons, with a large voltage difference between the anode and cathode used to create an avalanche. The total charge is collected on the anode, amplified by a preamplifier, and digitized by an fADC and read out by a DAQ. [6] 42

Comments

CHAPTER 1

INTRODUCTION

CHAPTER 2

ELECTRON-ION COLLIDER

It has been known for nearly a century that atoms are composed of nucleons (protons and neutrons), but it took another 50 years for Murray Gell-Mann and George Zweig to independently develop a model proposing that nucleons themselves are made up of constituent components, called quarks, bound together by the exchange of gluons [7]. This lead to the development of the fundamental theory of the strong interaction, known as Quantum Chromo-Dynamics (QCD). It is now a strong goal of the nuclear physics community to understand the interactions of quarks and gluons and how those interactions make manifest both nucleons themselves, which account for nearly all the mass of the visible matter in the universe, as well as the nucleons' spin, mass, magnetic moment, and nuclear binding energy. Because of the well-known properties of the electromagnetic interaction, electron scattering is an ideal process for such studies.

Although it would theoretically be possible to study these properties using fixed-target electron beam experiments, it is three-fold prohibitive: it is much more costly to construct an accelerator to accelerate electrons to the necessary momentum (on the order of TeV) than to build a collider, it is more difficult and complicated to do transverse nucleon polarization studies with a fixed target due to the nature of the required magnetic fields, and it is very difficult to study the target fragments of a fixed target reactions due to final state interactions whereas in a collider the fragments will be boosted in the same direction as the ion beam. It was therefore deemed a priority by the 2007 Nuclear Science Advisory Committee's Long-Range Plan that an Electron-Ion Collider (EIC) be the next facility to be built in the United States [8].

The EIC will not be the first facility to have the capability of colliding electrons and positrons with protons. The HERA accelerator in Hamburg, Germany was the world's first electron-proton collider, reaching electron energies of up to 28 GeV and protons to nearly 1 TeV with a luminosity on the order of 10^{31} cm^{-2} s^{-1} before shutting down in 2007. Figure 2.1 shows the combined H1 and Zeus experimental data from HERA for the measurement of the structure function for positron-proton scattering along with fixed target data for a wide range of both x and Q^2. The EIC hopes to improve upon the already rich science produced at HERA threefold: by increasing the luminosity of the accelerator to on the order of 10^{34} cm^{-2} s^{-1}, by allowing for the use of heavier ion beams such as oxygen, and by allowing for both transversely and longitudinally polarized beams of electrons and light ions. With these improvements the EIC will be able to look into hadronic final states with much greater detail.

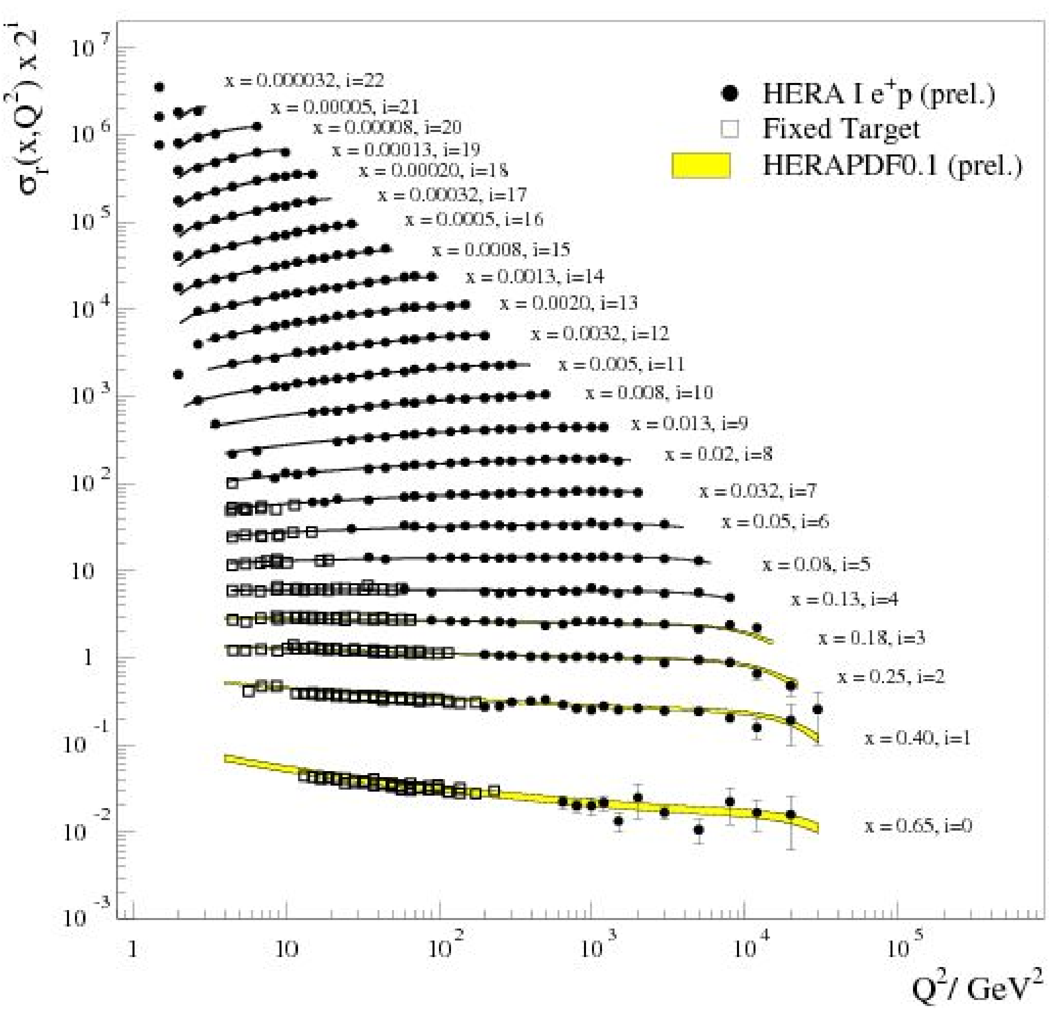

FIG. 2.1: The reduced cross section $\sigma_r(x, Q^2)$ as a function of Q^2. Filled circles are combined H1 and Zeus data from HERA for proton-positron collisions, hollow squares are from fixed target experiments, and the yellow is prediction from HERAPDF0.1. [1]

2.1 SCIENCE GOALS

The goal of an EIC will be to find out how QCD is responsible for the structure and dynamics of nucleons, the nature of the nucleon-nucleon force, and the relative importance of the valance quarks.

2.1.1 NUCLEON SPIN

One major question still pestering nuclear physicists is "What is the origin of the nucleon spin?". In the 1980s the naive answer was that the total nucleon spin was the sum of the spin of its three valance quarks, but many years of experimentation has revealed that it is much more complicated (Fig. 2.2), with the contributions both from quark and gluon spin and orbital angular momentum still in question. The EIC will be capable of much more detailed study of the contributions to the nucleon structure by enabling multi-dimensional projections of the distribution of quarks and gluons in space, longitudinal and transverse momenta, spin, and flavor.

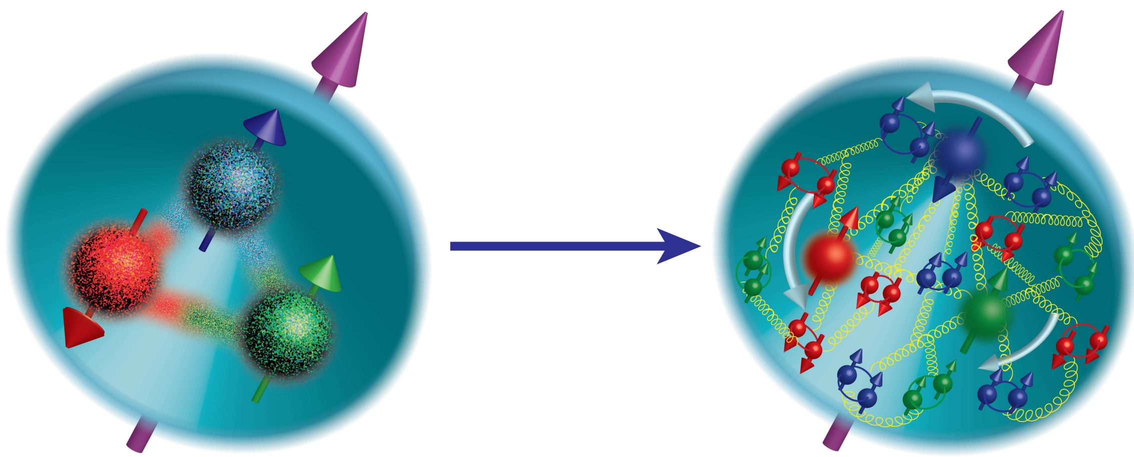

FIG. 2.2: Evolution of our understanding of nucleon spin structure. Left: In the 1980s, a nucleons spin was naively explained by the alignment of the spins of its constituent quarks. Right: In the current picture, valence quarks, sea quarks and gluons, and their possible orbital motion are expected to contribute to overall nucleon spin. [2]

2.1.2 THE EMC EFFECT

It was first observed by the European Muon Collaboration (EMC), and confirmed by other experiments that there is a modification between the nucleon structure function, F_2, of deuterium to those of heavier elements as a function of Bjorken x [9]. Figure 2.3 shows the ratios of the Deep Inelastic Scattering (DIS) cross sections of ^{3}He (top) to Deuterium and ^{4}He (bottom) to Deuterium as examples of this effect. Initial assumptions were that these cross section ratios would be unity, but measurements have clearly shown a suppression in this ratio for $0.3 < x < 0.8$, the now-called EMC Effect. One can also see an enhancement of the ratio for $0.1 < x < 0.3$ known as anti-shadowing, and the region of $x < 0.1$ where the ratio is again suppressed is the shadowing region.

The reason for this modification to the DIS cross section is still a mystery, but the EIC hopes to shed light on this phenomenon by studying various coherent exclusive reactions, such as J/Ψ production, which could allow for the quantification of initial conditions in heavy-ion collisions by mapping out the geometry of the nucleus in high-energy processes. This mapping can also help to understand other collective dynamics, such as the shadowing and anti-shadowing effects.

2.1.3 GLUON DISTRIBUTIONS INSIDE NUCLEI

As mentioned above, the EMC effect, the modification of the distribution of quarks in a nucleus versus their distribution in nucleons, is a known (yet still mysterious) phenomenon. It is suspected that this modification also occurs for gluons, with experiments such as ALICE showing evidence for gluon shadowing for $x \approx 10^{-3}$ [10]. The EIC hopes to measure this suppression of the structure functions thanks to its wider range of kinematics both in x and Q^2, allowing not only for the measurement of gluon shadowing ($x < 0.05$), but also anti-shadowing ($x \approx 0.1$), and possibly the EMC effect for gluons ($x > 0.3$), shedding light on the origins of the EMC effect.

2.2 FACILITIES

As of the writing of this thesis there are two competing designs for an EIC facility to be built in the United States: a figure-8 accelerator design for Thomas Jefferson National Accelerator Facility (JLab) (Figure 2.5), and a ring-ring accelerator design for Brookhaven National Lab (BNL) (Figure 2.6).

The JLab EIC (JLEIC) is planned to be approximately 1.4 km in circumference and have a footprint of roughly 500 m by 170 m. The design is a ring-ring with electrons and ions being stored in separate beam lines and collided at two interaction points (IPs) (outlined in red in Figure 2.5) on the figure-8. The JLab CEBAF SRF linac will be used as an electron injector for electrons with 3 - 11 GeV energy. The second ring will store an ion beam with energy of 20 to 100 GeV for protons or up to 40 GeV per nucleon for fully ionized light to heavy ions. The ion beams are generated and accelerated in a new ion injector complex with the same figure-8 design that will be utilized to preserve ion polarization. The two rings will be stacked vertically in the same underground tunnel [11].

The BNL facility, named eRHIC, will use a new electron beam facility based on an

Energy Recovery LINAC that will be built inside of the Relativistic Heavy Ion Collider (RHIC) tunnel to collide with RHIC's pre-existing polarized proton/ion beam. The existing hadron ring will accelerate protons up to 250 GeV/c, $^3He^{+2}$ up to 167 GeV/c per nucleon, and heavier ions (e.g. gold or uranium) up to 100 GeV/c per nucleon. The new electron ring will be capable of producing electrons from 2 - 21 GeV/c [12]. Figure 2.6 shows the current design layout of the eRHIC facility (top) and the Brookhaven eA Solenoidal Tracker (BeAST) detector proposed for the interaction region (bottom).

2.2.1 PARTICLE IDENTIFICATION REQUIREMENTS AND SOLUTIONS

The large center of mass energies and diverse physics program at an EIC necessitate a very sophisticated detector suite. The most basic process that the EIC will observe is inclusive DIS. This process will produce many different combinations of final-state hadrons over a wide angular distribution for a given kinematic setting of x and Q^2. Coupled with the large beam energies, there is a need of PID over a large range in the hadron endcap (up to 50 GeV/c), range up to the beam energy in the electron endcap (up to 12 GeV/c), and a moderate range in the central barrel region (up to 6 GeV/c). The ability to accurately identify hadrons in the final state is therefore a key requirement for the physics program, as is shown by Figure 2.4 which shows the momentum distributions of pions and kaons for each region of interest for typical beam energies for both BNL and JLab.

As can be seen in Figures 2.5 and 2.6, the layouts of the two detector concepts for JLab and BNL are slightly different, but the solutions for PID requirements are very similar. In the hadron endcap, because of the large final state energies the ideal PID detector would be a gaseous, mirror-based Ring Imaging Cherenkov (RICH) detector which would be capable of the required 50 GeV/c momentum resolution. The hadrons produced going towards the electron endcap scales in both energy and quantity with the energy of the electron beam energy. Although the maximum electron beam energies of JLab and BNL differ, a 10 GeV/c momentum resolution seems to be suitable for both facilities, and so a modular aerogel RICH detector is currently under development. In the central barrel region the necessary momentum coverage is not as high as that of the endcaps because the transferse momentum transfer from the electron beam to the ion beam is relatively small, on the order of 7 GeV/c. This smaller momentum range coupled with a smaller space to fit a detector make a detector based on Detection of Internally Reflected Cherenkov light (DIRC) technology, the main subject of this thesis, an ideal solution for PID in this region.

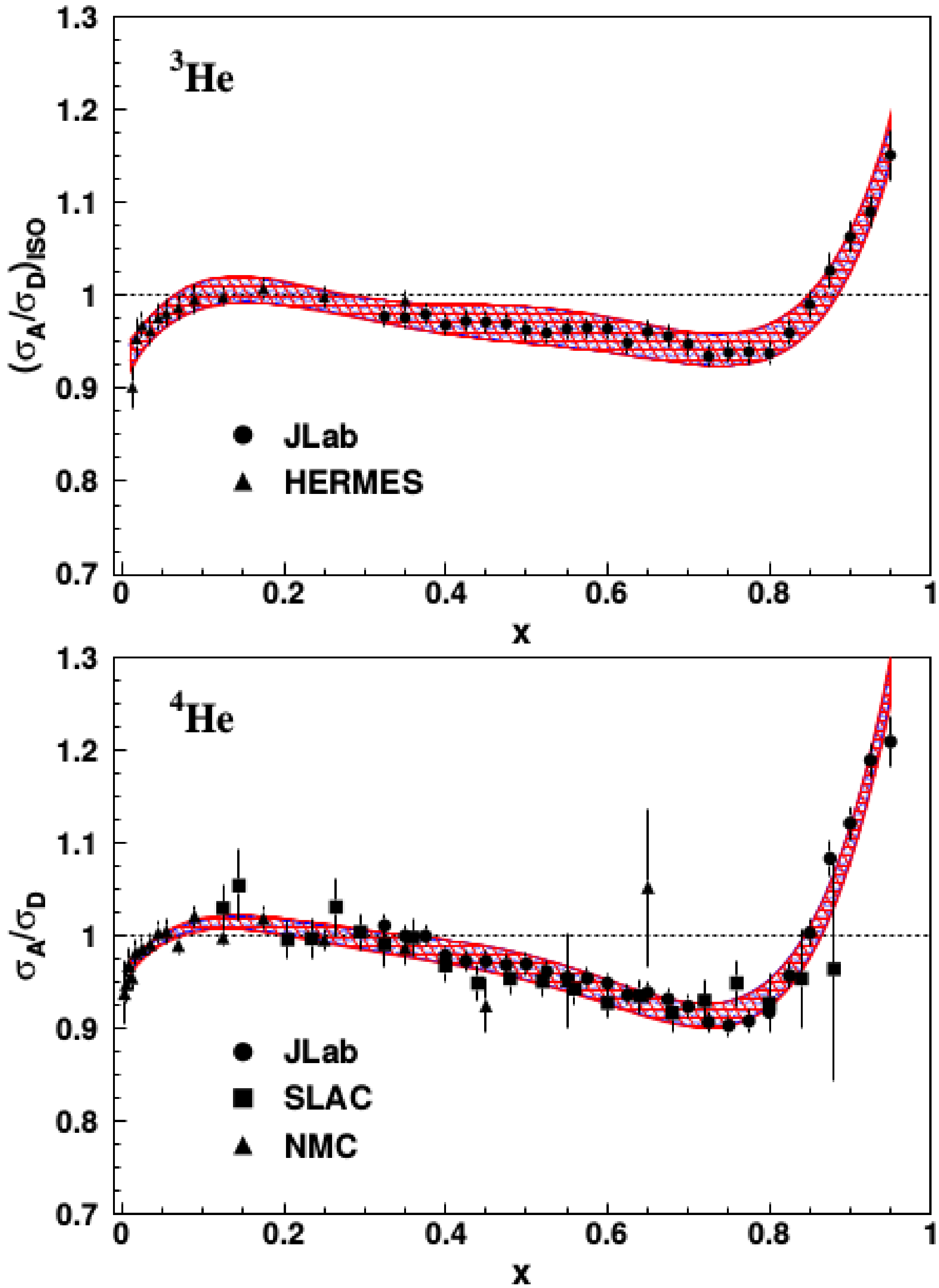

FIG. 2.3: Top: Ratios of ^{3}He to Deuterium DIS cross sections from JLab (circles) and HERMES (triangles). Bottom: Ratios of ^{4}He to Deuterium DIS cross sections from JLab (circles), SLAC (squares), and HERMES (triangles) [3].

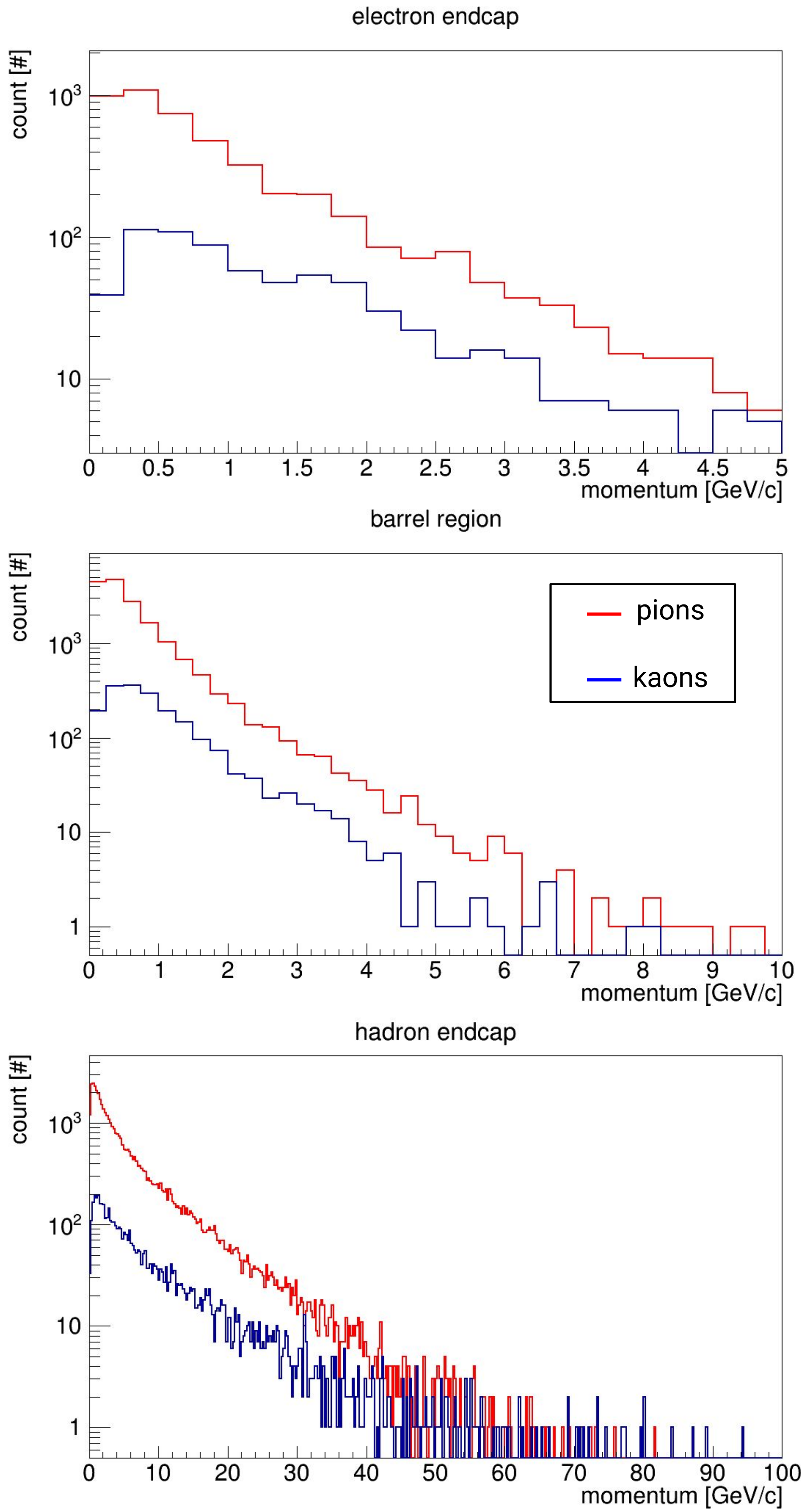

FIG. 2.4: Momentum distributions for pions (blue) and kaons (magenta) from the pythia simulation package for DIS events corresponding to collisions between 10 GeV electrons and 100 GeV protons, a common BNL/JLab kinematic, shown for a bin of $10 < Q2 < 100$ GeV^2.

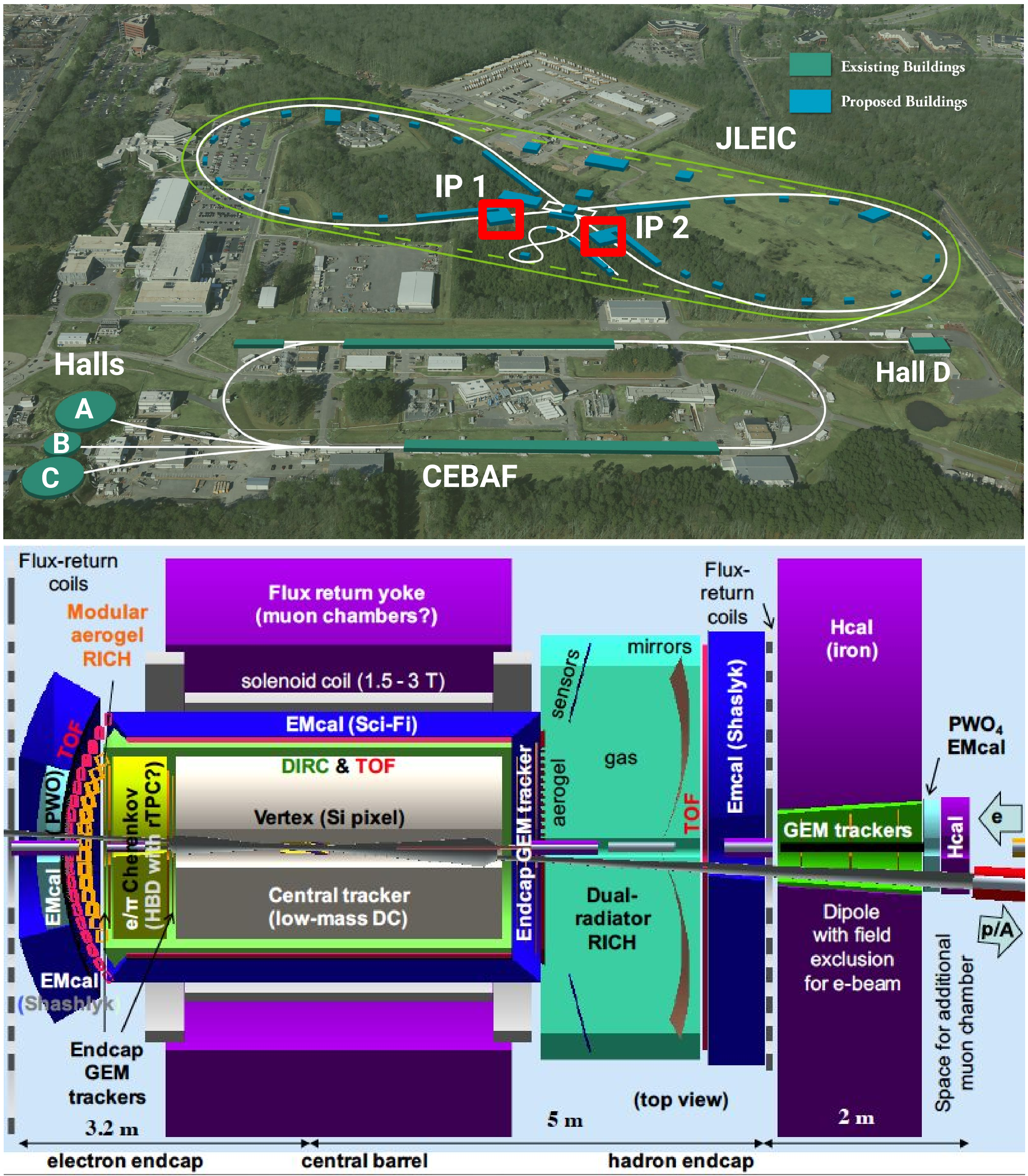

FIG. 2.5: Current design of the EIC facility for JLab with the two interaction points (IPs) highlighted in red (top), and the current baseline design for the detector at IP1 (bottom).

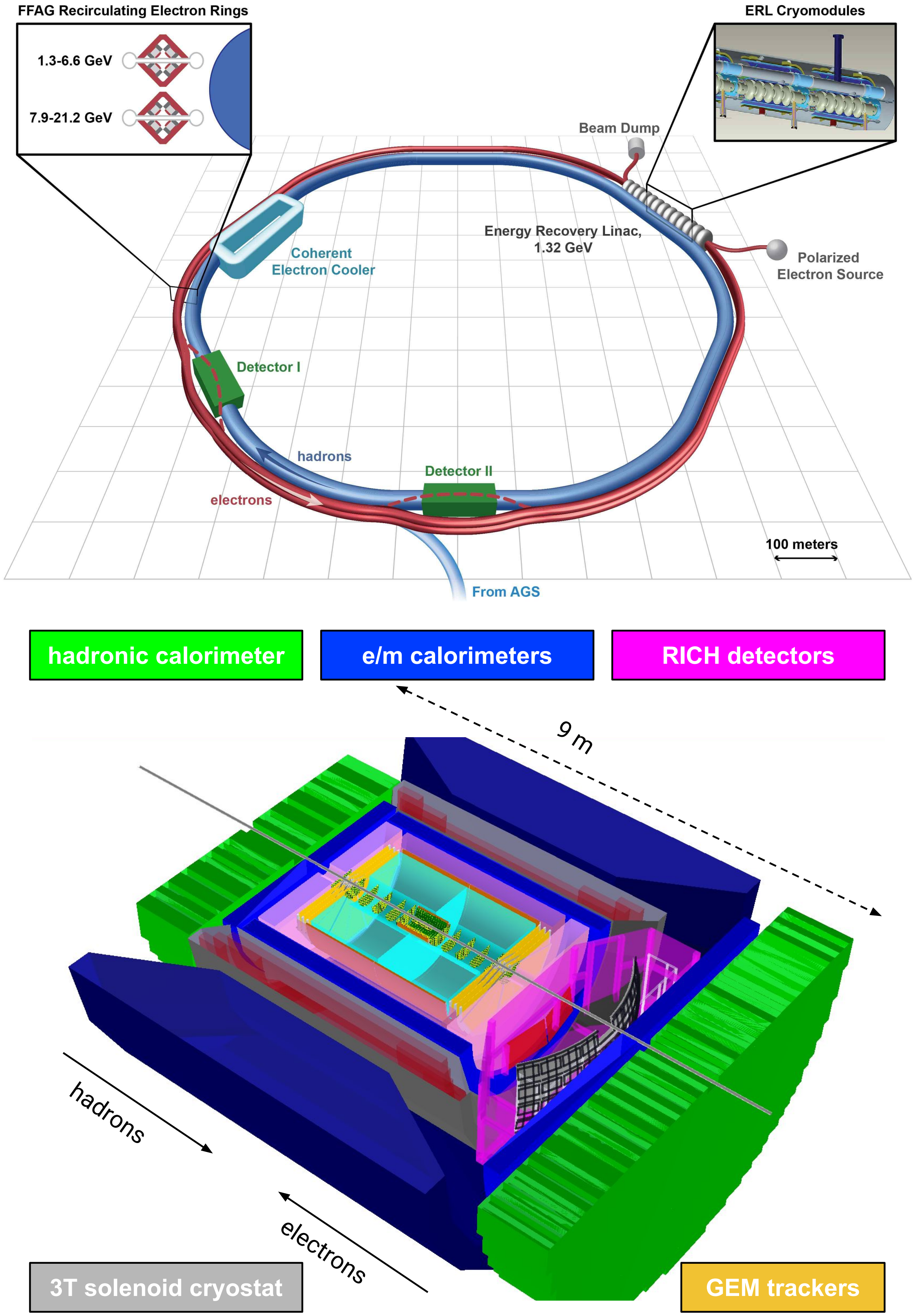

FIG. 2.6: Current design of the EIC facility at BNL (top), and the proposed BeAST (Brookhaven eA Solenoidal Tracker) detector (bottom).

CHAPTER 3

DIRC TECHNOLOGY

DIRC detectors are based on the concept of the Detection of Internally Reflected Cherenkov light (DIRC) produced in a solid radiator bar to identify charged particle. It is a special type of Cherenkov counter, which uses the unique properties of Cherenkov radiation to identify charged particle species.

3.1 CHERENKOV RADIATION

Einstein postulated in his Theory of Relativity that the speed of light in a vacuum, c, is the limit of the velocity of massive particles. In an optically transparent medium, however, the speed at which light propagates is modified: $c_{med} = c/n$, where n is the index of refraction of the medium. Pavel Cherenkov discovered in 1934 that massive particles moving through a medium faster than the speed of light in that medium emit light in the form of now-called Cherenkov radiation. Cherenkov was able to establish several interesting properties of this radiation: it is only emitted from charged particles above a certain velocity threshold $v > c/n$, the intensity is proportional to the particle's path length, emission is prompt, and the light is polarized with a continuous wavelength spectrum. Later in 1937 Ilya Frank and Igor Tamm theoretically formulated this radiation with fantastic agreement to Cherenkov's findings, and the three shared the 1958 Nobel Prize in Physics for their efforts [13].

Further studies confirmed that Cherenkov radiation is emitted uniformly in azimuth (ϕ_c) around the particle's direction of travel with the polar opening angle θ_C defined as

$$\cos\theta_C = \frac{1}{\beta n(\lambda)}, \tag{3.1}$$

where $\beta = v_p/c$, v_p is the particle's velocity, and the index of refraction is a function of the emitted photon wavelength. In a normal, dispersive optical medium the opening half-angle of the shock wave produced by the Cherenkov radiation, η_C defined in Figure 3.1, is not complementary to the Cherenkov angle. The relationship between the two is given by

$$\cot\eta_C = \left[\frac{\mathrm{d}}{\mathrm{d}\omega}(\omega\tan\theta_C)\right]_{\omega_0} = \left[\tan\theta_C + \beta^2\omega n(\omega)\frac{\mathrm{d}n}{\mathrm{d}\omega}\cot\theta_C\right]_{\omega_0} \tag{3.2}$$

where ω_0 is the central vale of the considered frequency range. Because the second term in (3.2) is zero only for non-dispersive media the shock wave front is not perpendicular to the Cherenkov cone in real detectors.

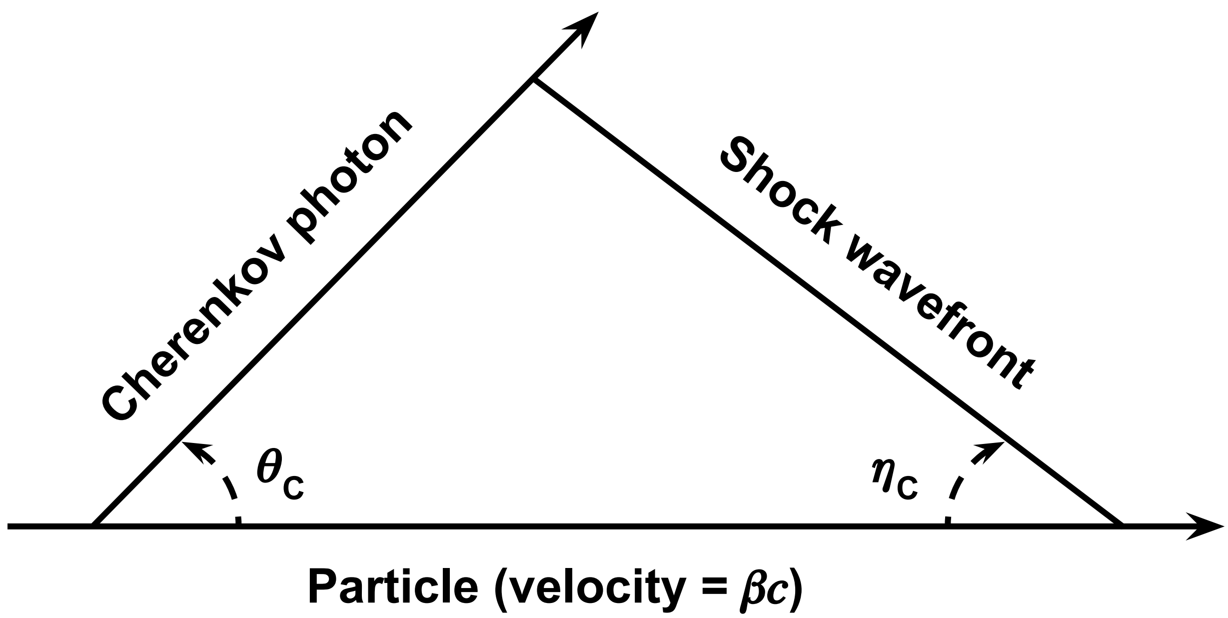

FIG. 3.1: Illustration of the Cherenkov cone.

Because particles lose very little energy when radiating Cherenkov photons the emission is very weak. The number of photons $N_{photons}$ emitted per path length L (in cm) by a moving particle with charge z is given by the Frank-Tamm equation

$$\frac{N_{photons}}{L} = \frac{\alpha^2 z^2}{r_e m_e c^2} \int \sin^2 \theta_C(E) \mathrm{d}E \tag{3.3}$$

where E is the photon energy in eV, the integral is taken over the region where $n(E)$ is greater than 1, and $\frac{\alpha^2 z^2}{r_e m_e c^2} = 370 \text{ cm}^{-1} \text{ eV}^{-1}$.

3.2 APPLYING THE CHERENKOV EFFECT TO PARTICLE ID

In order to identify particle species one must know both the mass and charge of the particle in question. Because the Cherenkov angle encodes the particle's velocity it is, in principle, a simple matter to measure the particle's momentum with a tracking chamber as well as the velocity obtained from (3.1) to determine the mass and charge. Figure 3.2 shows how different particle species can be distinguished for a given momentum in fused silica.

Threshold counters are Cherenkov detectors used for particle identification (PID) by exploiting the fact that only particles above the threshold velocity $\beta > 1/n$ will emit Cherenkov photons. Therefore lighter particles will emit Cherenkov light while heavier particles will not for a given momentum. The information about a particle's velocity can be combined with momentum information from a tracking system to determine the mass as [14]

$$m = \frac{p}{c}\sqrt{n^2 \cos^2 \theta_C - 1} \tag{3.4}$$

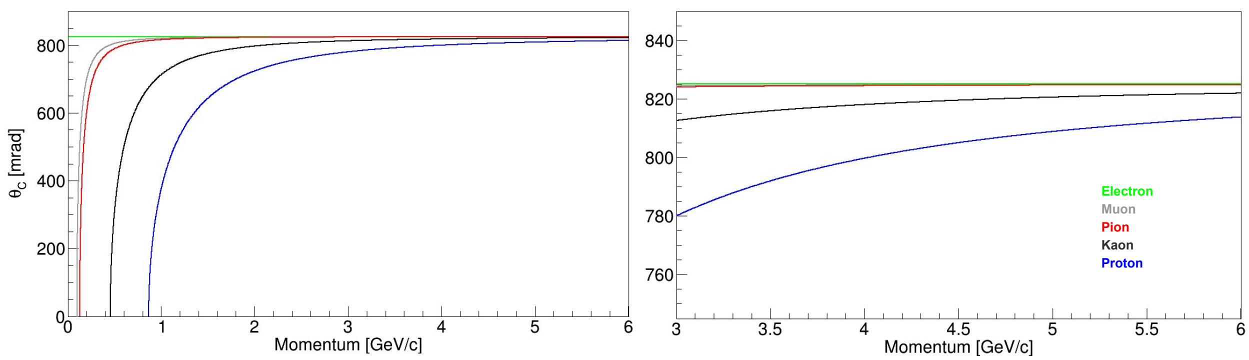

FIG. 3.2: Particle momentum [GeV/c] versus Cherenkov angle [mrad] for different particle species in fused silica ($n \approx 1.473$). While the full range (left) makes it seem as if separation between heavier species becomes more and more challenging, zooming in (right) shows that it is indeed possible separate protons, kaons, and pions even at higher particle momentum.

3.3 RING IMAGING DETECTORS

Ring Imaging Cherenkov (RICH) detectors are designed to efficiently identify and separate different particle species over a wide range of momenta. A basic RICH system is shown in Figure 3.3.

A volume of radiator, either gaseous (e.g. C_4F_{10}) or solid (e.g. aerogel), is positioned upstream of an array of photosensors. A charged particle traveling through a thin radiator above the threshold velocity will continuously emit Cherenkov photons in a cone. The resulting image on the photosensor array is an annulus of thickness $d \tan\theta_C$ and an inner radius of $L \tan\theta_C$, where d is the distance the particle traveled inside the radiator, L is the distance between the radiator and the photosensors, and θ_C is the usual Cherenkov angle (Figure 3.3b). PID is done by measuring the average radius of the annulus and reconstructing the Cherenkov angle geometrically.

3.4 DIRC DETECTORS

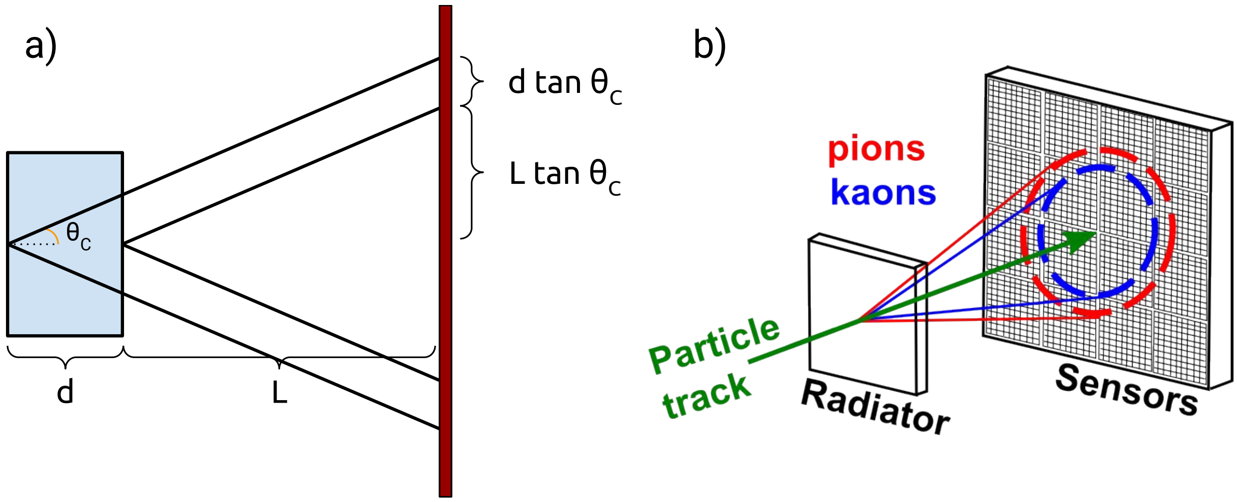

FIG. 3.3: Basic concept of a proximity focusing Ring Imaging Cherenkov (RICH) detector (a), and an example of how they can be used to do PID based on particle mass (b).

DIRC detectors work much the same way as a RICH in that they collect Cherenkov photons produced from a radiating material and use the created image on the photosensors to reconstruct the Cherenkov angle. In the case of a DIRC, the radiating medium is also used as a light guide as some of the Cherenkov photons undergo total internal reflection inside the radiator and are guided towards one end of the radiator to a readout (Figure 3.4). The radiator of choice is a solid bar made of fused silica, with an index of refraction $n \approx 1.473$. A rectangular cross section and highly smoothed and polished sides ensure that the magnitude of the Cherenkov angle is preserved during internal reflection. Photons that are created propagating away from the readout are reflected back towards the readout by a mirror. Once the photons exit the radiator they are allowed to separate through an expansion volume before being imaged in both (x, y) position as well as time. The arrival position and propagation time of each detected photon are combined with tracking information to reconstruct the Cherenkov angle and determine the corresponding PID likelihoods (reconstruction methods and techniques for DIRC detectors will be discussed in detail in Chapter 6).

The performance of a DIRC detector is given by the resolution in the Cherenkov polar opening angle of the particle track, $\sigma^2_{\theta_C,\mathrm{track}}$, which can be written as:

$$\sigma^2_{\theta_C,\mathrm{track}} = \sigma^2_{\theta_C}/N_\gamma + \sigma^2_{\mathrm{correlated}} \tag{3.5}$$

where σ_{θ_C} is the average single photon Cherenkov angle resolution, N_γ is the number of

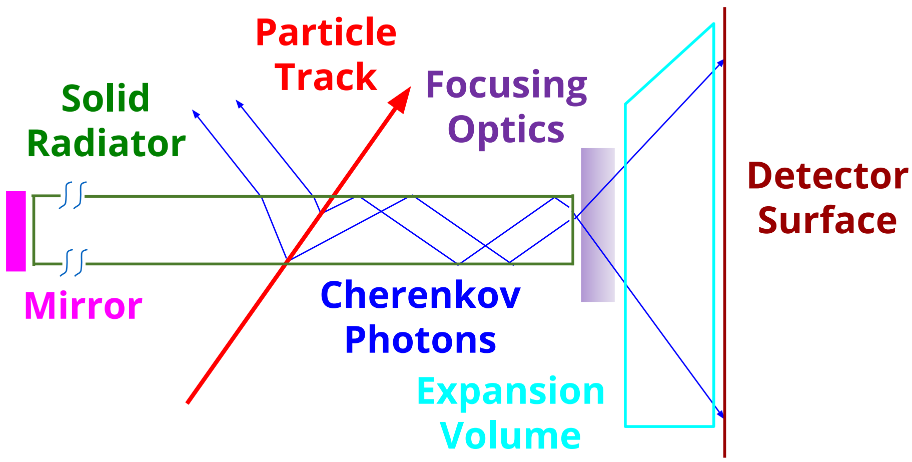

FIG. 3.4: The basic components of a DIRC detector: a solid radiator, typically fused silica (green); a mirror to redirect backward-going photons (pink); optional focusing optics (purple); an expansion volume to allow photons to separate in space (cyan); and a detector surface to record the position and arrival time of Cherenkov photons (blue).

measured photons per track, and $\sigma_{\text{correlated}}$ includes several correlated terms that contribute to the resolution such as the uncertainty in the particle track direction coming from external tracking systems. Because the track direction is crucial to the reconstruction of the Cherenkov angle, this error needs to be small for the performance to not suffer. For the EIC a tracking resolution on the order of 1 mrad is required for adequate PID.

As of the writing of this thesis the only DIRC detector used in a full experiment is the BaBar DIRC at SLAC National Accelerator Laboratory, which was successfully operated from 1999 through 2008 [15]. It proved to be a robust, stable, and easy to operate system for more than 8 years, providing excellent pion/kaon separation for all tracks from B-meson decays. It used 4.9 m long radiator bars with a rectangular cross section of 17.25×35 mm^2. Each bar was made of four 1.225 m long fused silica bars glued end-to-end. The bars were placed in 12 hermetically sealed containers, called bar boxes, each holding 12 radiator bars for a total of 144 bars. At the end of each box was attached a wedge of fused silica and a window to allow the photons to expand before entering the water-filled expansion volume and being read out on one of 10,752 photomultiplier tubes (see Figure 3.5). Figure 3.6 summarizes the performance of the BaBar DIRC, showing excellent Cherenkov angle reconstruction (2.5 mrad, only 14% larger than the design goal of 2.2 mrad) and photon yield per track.

3.4.1 DIRCS IN FUTURE EXPERIMENTS

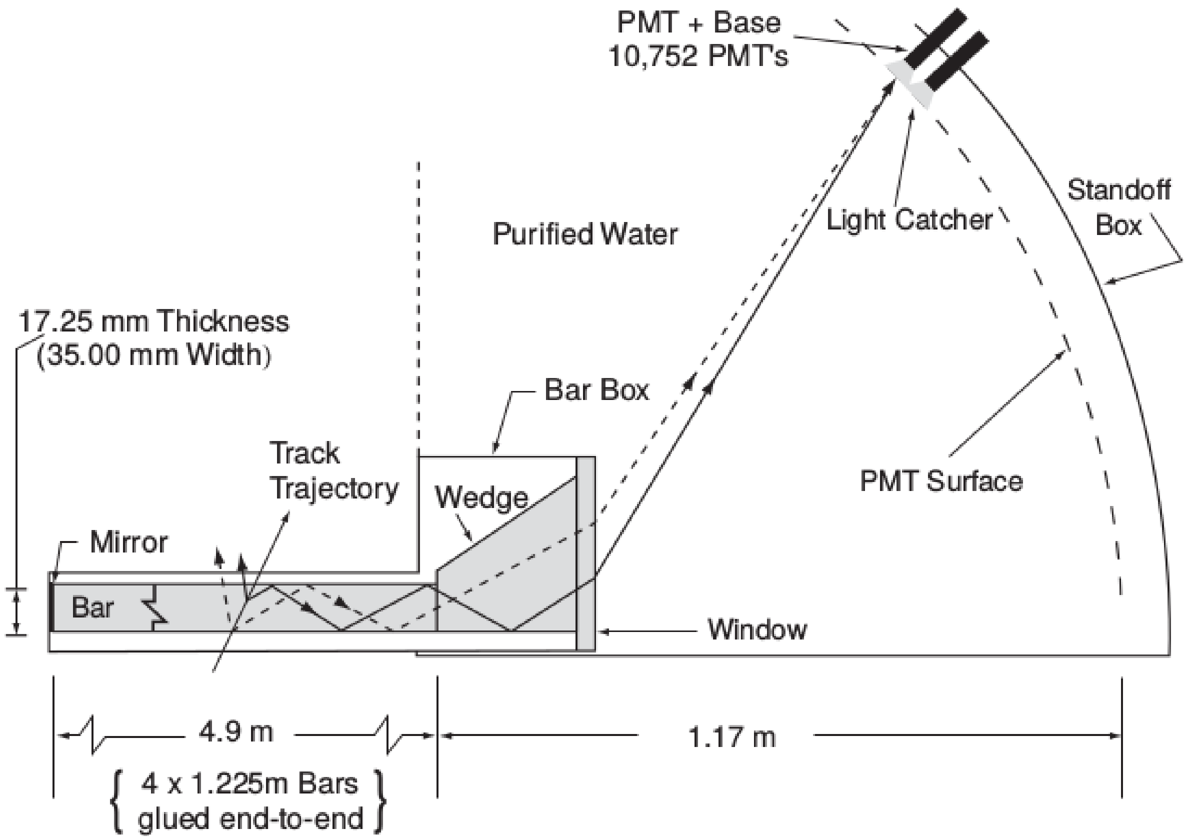

FIG. 3.5: Schematic of BaBar DIRC and detection region.

The BaBar DIRC has since inspired many other experiments/facilities, including the EIC, to utilize this new, novel PID system in a variety of ways (Figure 3.7). The Focusing DIRC (FDIRC) proposed for the now-cancelled SuperB collider in Italy was the first to propose using some form of focusing for the Cherenkov photons, allowing for a factor of 10 smaller expansion volume [16]. The barrel DIRC for the PANDA experiment at FAIR in Germany will use shorter radiator bars for a more compact design [5], while the PANDA disc DIRC will be used in the forward region and will be the first disc DIRC to be used in a high-performance 4π detector [17]. Belle II at the SuperKEKB accelerator in Japan will utilize wide plates as radiators and focus on fast timing for PID in the barrel region [18]. The TORCH detector, similar to the PANDA disc DIRC, will be a large-area detector focusing on precision time-of-flight to do PID for low momentum kaons at the upgraded LHCb experiment [19]. The GlueX experiment at JLab will be recycling four bar boxes from the BaBar experiment to cover the forward region of their spectrometer; utilizing focusing

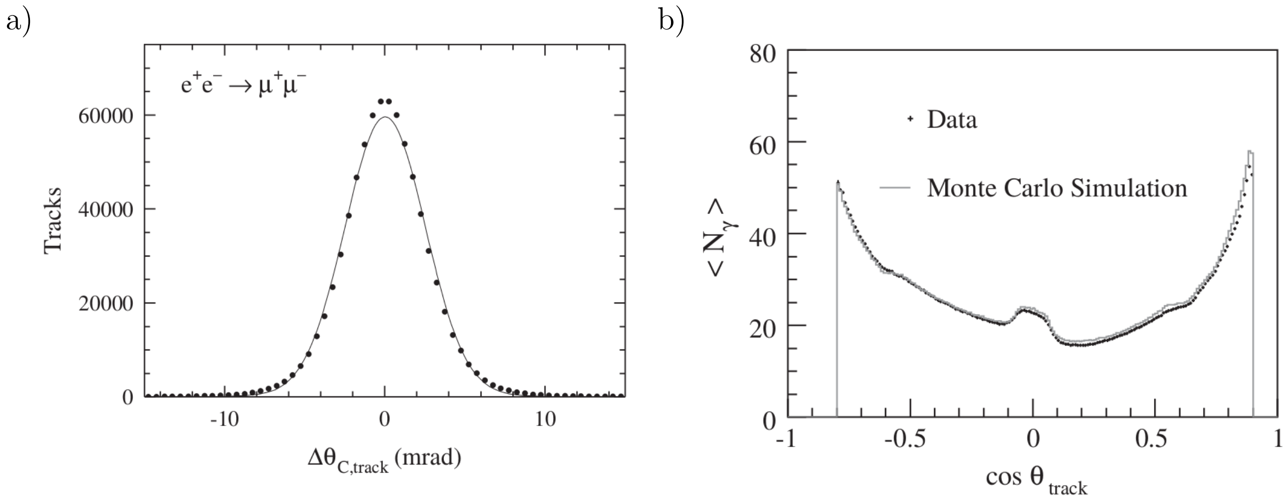

FIG. 3.6: Performance of the BaBar DIRC for $e^+e^- \to \mu^+\mu^-$ events. a) shows the difference between the measured and expected Cherenkov angle (dots) and a Gaussian fit to the data with a 2.5 mrad width (line). b) is the average number of detected photons vs. track polar angle for data (dots) and Geant4 [4] simulation (line).

similar to the FDIRC design [20].

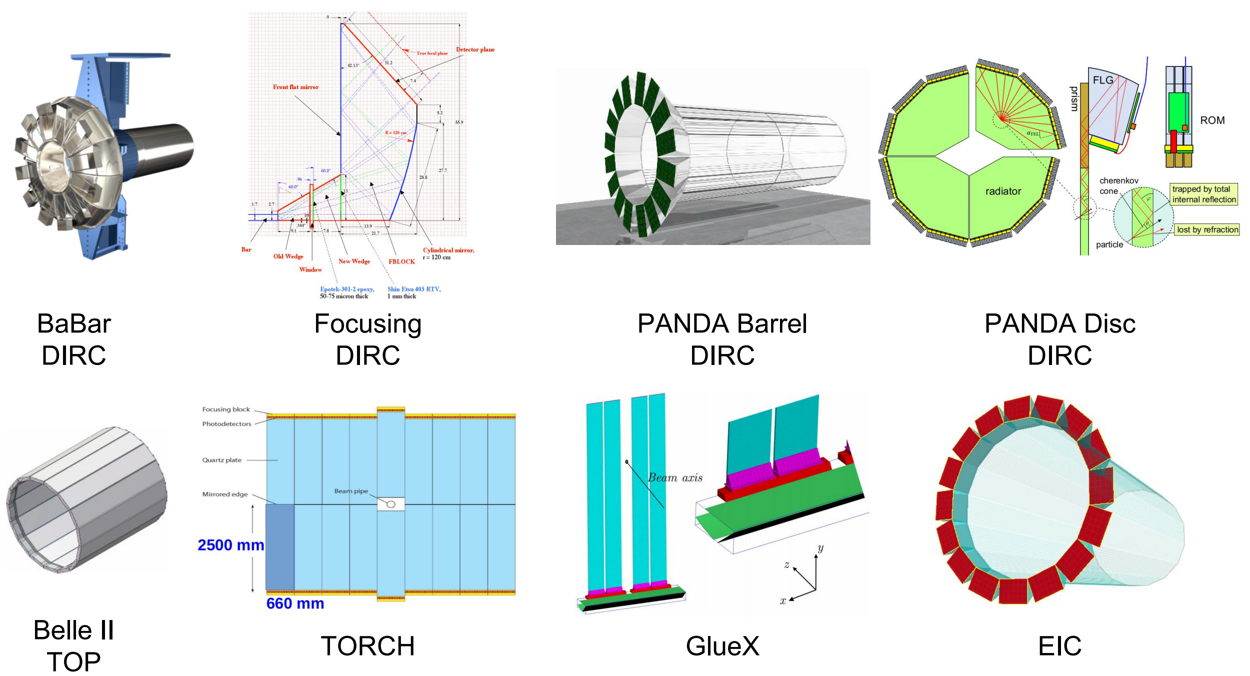

FIG. 3.7: Evolution of the DIRC concept. From top left to bottom right: BaBar Barrel DIRC, Focusing DIRC, PANDA Barrel DIRC, PANDA Disc DIRC, Belle II Time of Propagation DIRC, LHCb TORCH DIRC, GlueX DIRC, EIC DIRC

3.5 HIT PATTERNS AND PARTICLE SEPARATION METHODS

As mentioned previously, a DIRC detector is a compact RICH system that relies on internal reflection of the Cherenkov photons in the radiating material. However, as is illustrated in Figure 3.4, not all of the light produced inside the radiator is internally reflected as photons with an angle less than the critical angle (approximately 43° for the interface from fused silica to air) with respect to the surface will escape the radiator. Because of this loss of photons the hit patter of a DIRC is only roughly half of a typical RICH ring, which is then mirrored depending on where the photon exited the radiator. If the expansion volume is more radially compact the two ring segments become stacked side by side. To complicate matters further, if the expansion volume is small enough that reflections from the sides occur then the ring segments are folded on top of themselves to create much more complicated hit patterns. Figure 3.8 illustrates this folding of the hit pattern due to expansion volume size. Figure 3.9 shows the contribution to the folded pattern from single reflections inside a prism shaped expansion volume.

Two approaches were used in the analysis presented in this thesis for particle species separation: reconstruction of the Cherenkov angle using a geometrical reconstruction method similar to the one used by the BaBar DIRC, and time-based imaging using probability density functions (PDFs) similar to that used by the Belle II Time of Propagation counter.

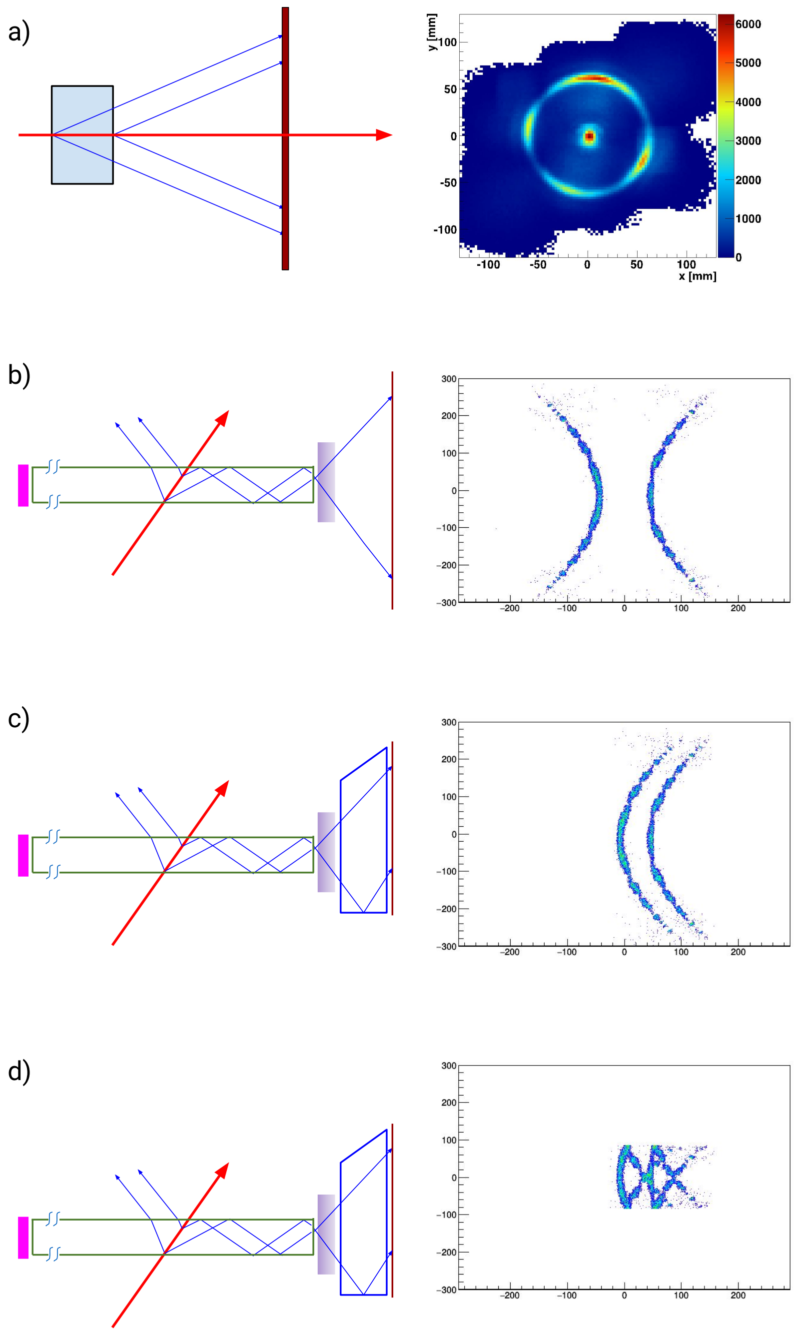

FIG. 3.8: Various detector geometries (left) and the resulting simulated hit patterns (right) from 1000 identical particles. A typical RICH detector (a), produces a very nice ring pattern. A DIRC detector with a sufficiently large expansion volume using a thin radiator bar (b) produces two ring segments. A DIRC with a radially compact expansion volume (c) will reflect one of the ring segments so that it will stack side by side. Finally, a DIRC detector with a compact expansion volume both radially and transversely (i.e. into and out of the page) (d) will cause the ring segments to fold in on themselves, making a fish-like pattern. The DIRC patterns are viewed from the back of the detector plane and rotated 90° clockwise relative to the corresponding geometry.

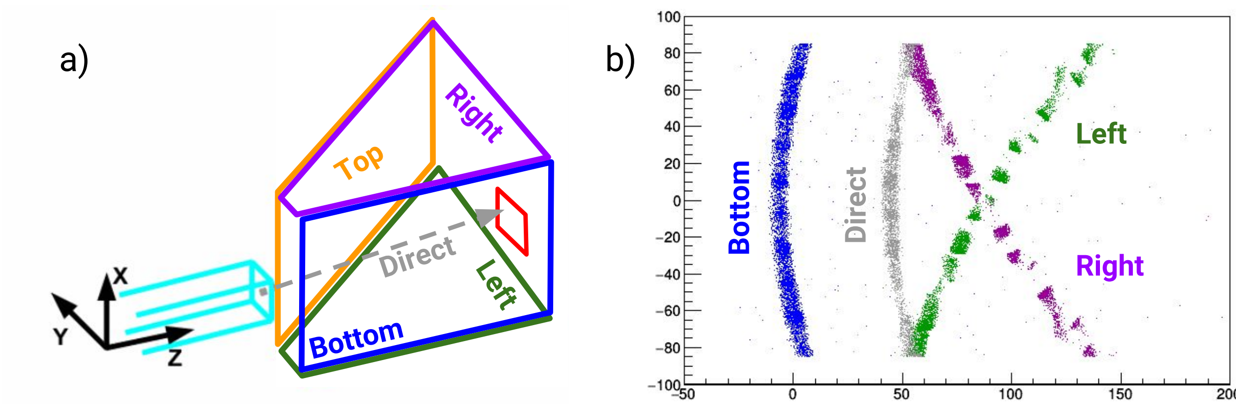

FIG. 3.9: For a prism-shaped expansion volume (a) different segments of the hit pattern correspond to different paths taken (b). Paths with multiple reflections inside the prism (e.g. bottom-left) have been excluded for simplicity.

3.5.1 CHERENKOV ANGLE RECONSTRUCTION

The emmission angle between a single photon and the particle track can be reconstructed from the observed photon coordinates on the detector plane. The spacial position of the centers of the radiator bar and the struck pixel are known and used to define the 3-dimensional direction vector $\vec{k} = (k_x, k_y, k_z)$ pointing from the center of the bar end to the center of the pixel (shown in Figure 3.10) . The k-vector is defined as the photon exit vector just inside the bar. The direction vector from the bar center to the pixel center along with Snell's law are used to determine the k-vector. Together with the particle direction $\vec{p} = (p_x, p_y, p_z)$ the Cherenkov angle for each photon can be calculated from

$$\theta_C = \arccos\left(\frac{\vec{k} \times \vec{p}}{|p|}\right) \tag{3.6}$$

In order to get a value of the k-vector for each pixel a photon gun is used in Geant4 to illuminate the detector plane. Roughly 10^5 photons are created at the end of the bar uniformly and allowed to propagate through the expansion volume and onto the photosensors. The initial value of the k-vector, the propagation time, number of bounces inside the expansion volume, and sensor and pixel number are all stored in large table, called a "look-up" table. The values in the lookup table are independent of particle species and momentum and only depends upon the detector geometry (e.g. the focusing optic, or the location of the bar relative to the expansion volume). Because of this a look-up table for a given geometry can be generated before taking data. Another advantage to the geometrical reconstruction is

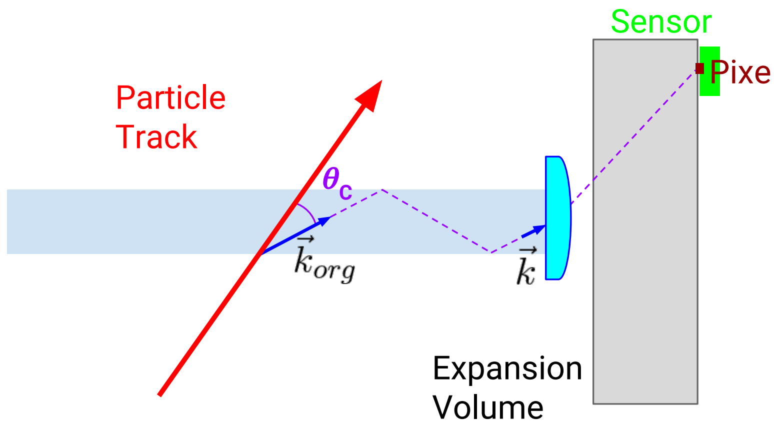

FIG. 3.10: Schematic of the geometric reconstruction concept, with a photon (purple) being emitted from the particle track. The direction of the k-vector can be used to determine the original direction vector, $\vec{k}_{org}$, of the photon and is used for the reconstruction of θ_C.

that a full simulation of the particle track is not needed which saves a lot of computation, as much of the computing power used during a simulation is used for the photon propagation through the bar.

Unfortunately, the direction of the k-vector as reconstructed by the pixel does not uniquely define the directionality of $\vec{k}_{org}$. Unfortunately, this method only offers an approximation to the magnitude of the k-vector. Because the number of reflections inside the bar cannot be known there are 8 possibilities, or ambiguities, for the original directionality of the photon that must be considered (forward/backward, up/down, and left/right). Figure 3.11 illustrates a 2D simplification of this problem, showing 4 possible photon directions propagating from the particle track. Here each of θ_{1-4} are possible values for the true Cherenkov angle. In the full 3D space this leads to up to 8 possibilities to be considered for the k-vector for each detected photon, and therefore up to 8 values of the Cherenkov angle θ_C.

In addition to ambiguities coming from guessing the initial directionality of the k-vector inside the bar there are also ambiguities coming from the multiple possible paths that a photon could take from the center of the bar to a pixel inside the expansion volume. Figure 3.13 shows a prism-shaped expansion volume, similar to that used in the analysis presented later in Chapter 6, showing the labeling of the surfaces and an example of ambiguous photon paths from the bar to a pixel on the detector plane.

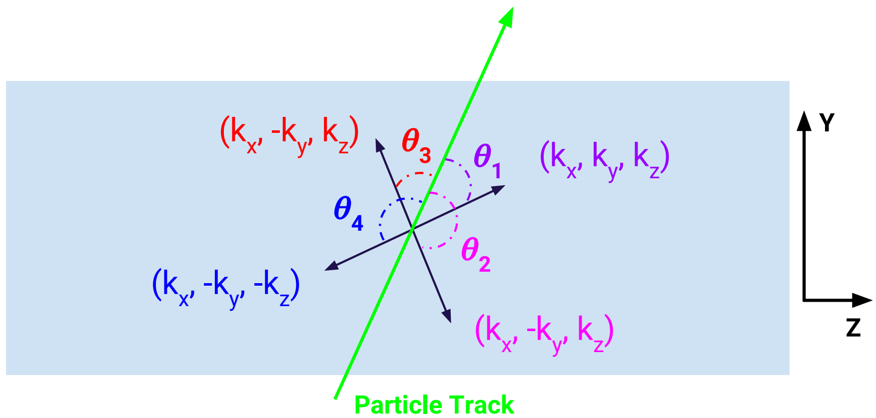

FIG. 3.11: 2D illustration showing all possible combinations of k-vector directions off of the particle track. Not shown are the additional 4 components where $k_x \rightarrow -k_x$.

The number of ambiguous paths that are reconstructed can be reduced by averaging the initial direction of all photons in the lookup table that have the same number and types of reflections and land in the same pixel. As a simplified example, see Figure 3.12

The Cherenkov angle is not, however, only reconstructed for one photon, but for up to 160 photons per particle track. For each photon at least one of these reconstructed θ_C values is correct, while the others contribute to a combinatorial background in a spectrum of the reconstructed angle, an example of which can be seen in Figure 3.14 for 7 GeV/c protons with a 125° polar angle and made with an averaged path lookup table.

3.5.2 TIME-BASED IMAGING

The other method of particle species separation that can be used for a DIRC is time-based imaging or time-based reconstruction, similar to that used by the Belle II Time-Of-Propagation counter. The full Geant4 simulation is used to record the arrival time of photons for each particle species of interest, which are the stored in an array of normalized histograms to produce PDFs [5].

For each track the photon arrival time for each pixel with a recorded hit is compared to the PDF for each particle species, and the time-based likelihood is calculated as $L = ln(h)$ where h is the value of the PDF for the photon arrival time for a given particle hypothesis. One can then compare the likelihoods of different particle species to get a separation power for particle identification. The separation power for time-based reconstruction between two particle species is given by the magnitude of the difference of the two log likelihood plots

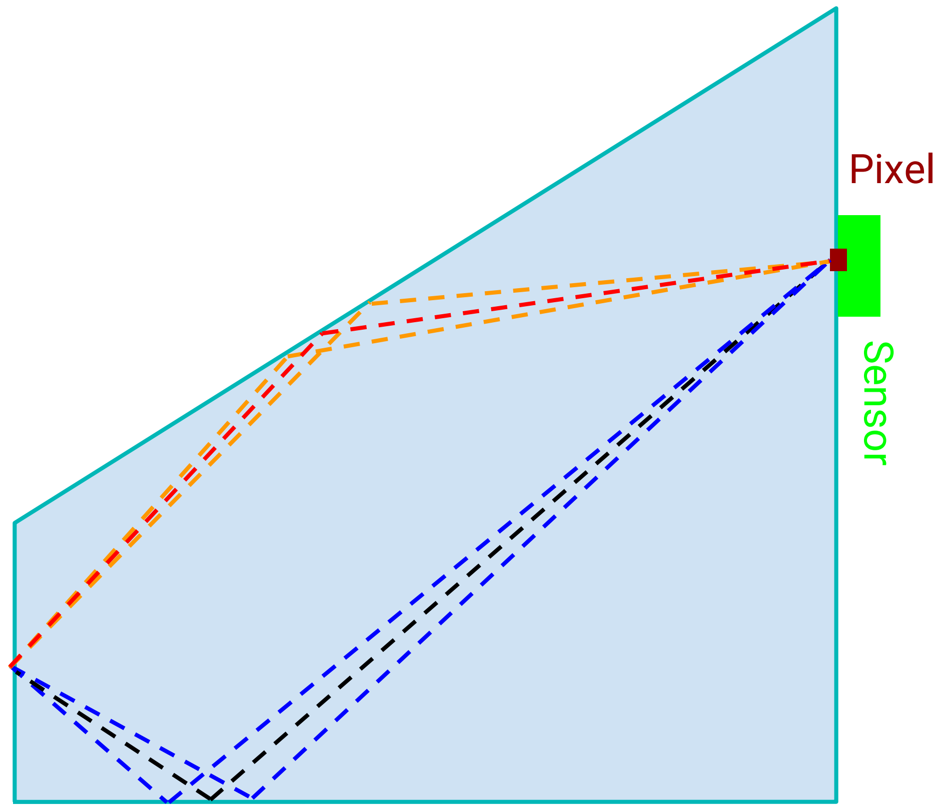

FIG. 3.12: 2D example of averaging LUT entries to reduce prism ambiguity reconstructions. The two photons reflecting off of the bottom prism face (blue) have been averaged to the one black photon. The two photons reflecting off of the top prism face (orange) have been average to the red photon. In this simplified example the number of entries in the lookup table have been reduced by half. Angles have been exaggerated.

divided by the average sigma. An example of time-based reconstruction for a bar radiator with a prism expansion volume is shown in Figure 3.15 for pions and kaons in a plate radiator with a prism expansion volume.

This method of particle separation is also very useful for plate-type radiators as the lookup tables in the geometric reconstruction assume the photons come from the center of the bar, which is no longer a good assumption for wide plates.

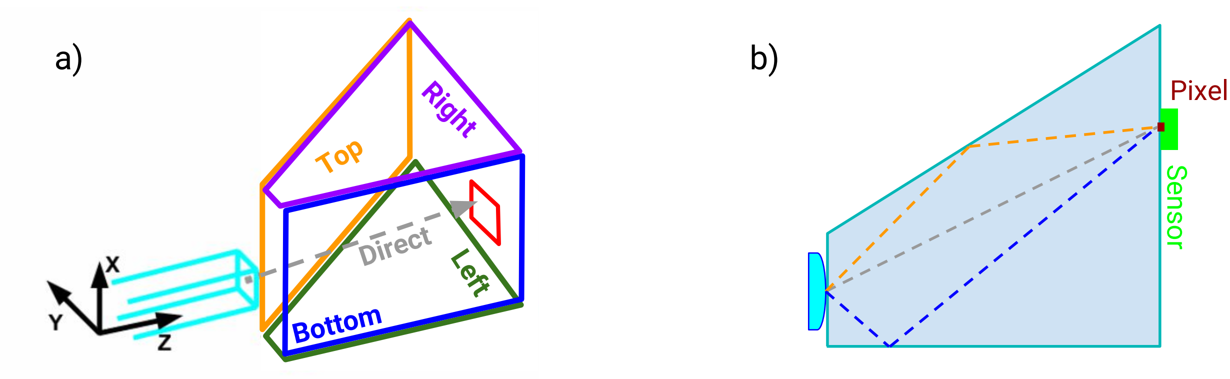

FIG. 3.13: Illustration of possible ambiguities in the θ_C reconstruction coming from possible paths in a prism-shaped expansion volume. Each face is labeled in a) along with an example of a direct path, while b) shows 3 possible paths that lead from the bar to a certain pixel: 1 top reflection (gold), 1 bottom reflection (blue), and 1 direct path (gray).

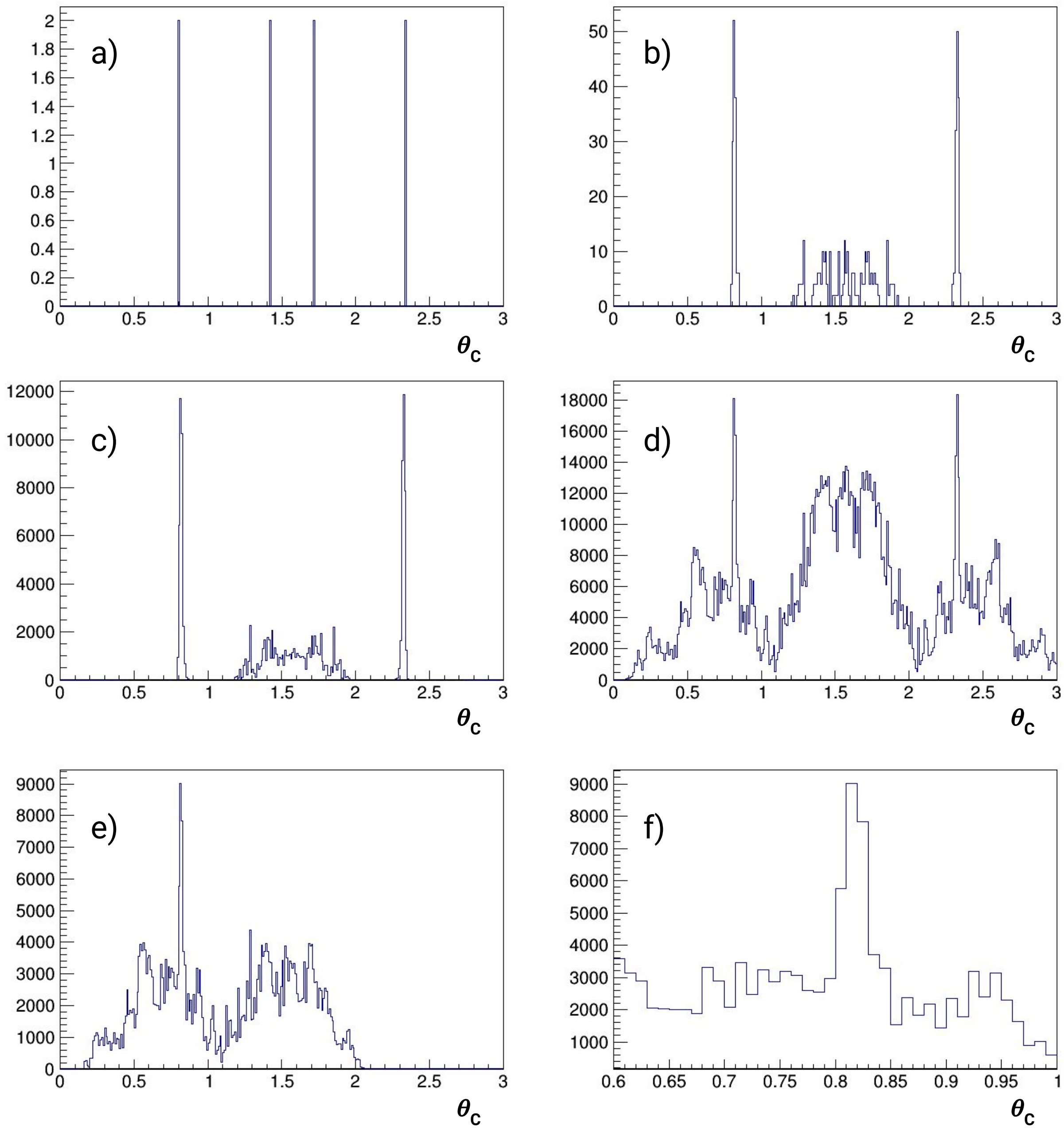

FIG. 3.14: Simulated reconstructed Cherenkov angle per photon from a 7 GeV/c particle with a polar angle of 125° for: a) one photon from a proton with only bar ambiguities, b) all photons from one proton with only bar ambiguities, c) all photons from 1000 identical protons with only bar ambiguities, d) all photons from 1000 identical protons with both bar and prism ambiguities, e) same as d) but with constraints on the photon angle with the bar surface and neglecting y direction flips due to zero beam divergence, and f) a zoom showing a buildup around the calculated value of 816 mrad along with a combinatorial background.

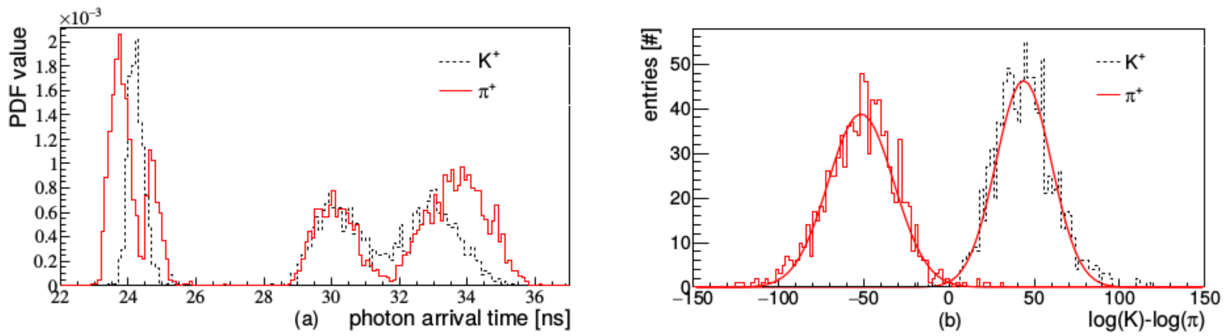

FIG. 3.15: Example time-based reconstruction for a plate radiator with a prism expansion volume for kaons (dashed) and pions (red). Photon arrival times for one MCP-PMT pixel are shown in a), and b) is the log-likelihood difference for kaon and pion hypotheses for a smaple of 3.5 GeV/c particles at 22° polar angle [5].

CHAPTER 4

HIGH-PERFORMANCE DIRC@EIC

The BaBar DIRC was able to reach a performance of 3 standard deviations (s.d.) separation for pions and kaons at up to 4 GeV/c particle momentum. PANDA Barrel DIRC wishes to achieve similar performance, but due to space constraints they will be using a smaller expansion volume and must therefore rely on optical focusing of the Cherenkov photons to reach this performance. In both cases the separation power requires a per track Cherenkov angle resolution (Eq. 3.5) of 2.5 mrad The physics goals of an EIC require a pion/kaon separation of 3 s.d. at up to 6 GeV/c momentum, which requires 1 mrad track Cherenkov angle resolution. The graph in Figure 4.1 shows pion-kaon separation as a function of particle momentum for different assumptions of the per track Cherenkov angle resolution, highlighting the achieved performance of BaBar and the desired performance of PANDA and EIC. In order to reach this high resolution in a compact space the EIC DIRC must incorporate cutting-edge technology in focusing optics and photo sensor granularity and timing resolution.

4.1 HIGH-PERFORMANCE DIRC COMPONENTS AND DESIGN

The baseline design of a DIRC for EIC has been constructed in a Geant4 simulation, as shown in Figure 4.2. There are 16 modules, called bar boxes, each containing 11 radiator bars 4200 mm long with a cross section of 17×35.4 mm^2. The 16 bar boxes are arranged in a barrel with a radius of 1 m around the beam line. Mirrors are coupled to one end of each bar, and a special 3-layer lens, discussed in more detail later, is attached to the other end. The lens is then coupled directly to a prism-shaped expansion volume made of fused silica, the same material as the radiator bars. The prism has an opening angle of 38° with dimensions of $284.3 \times 390 \times 300$ mm^3. The 284.3×390 mm^2 detector plane of each prism is covered with micro-channel plate photomultiplier tubes (MCP-PMTs) with 27,690 2×2 mm^2 pixels, for a total of 443,040 channels across the entire detector to record the location and arrival time of each detected Cherenkov photon.

4.1.1 FOCUSING OPTICS

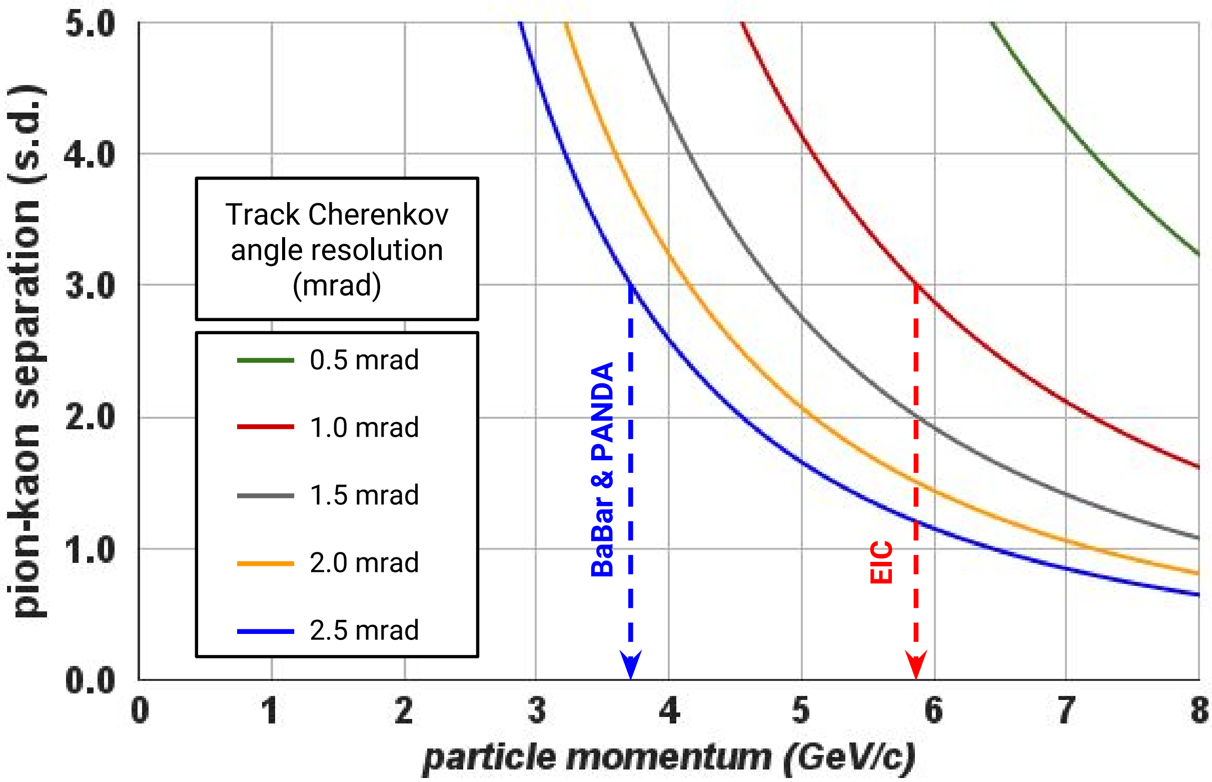

FIG. 4.1: Pion-kaon separation as a function of particle momentum for different assumptions of the per track Cherenkov angle resolution. The PID requirements of the EIC necessitate a per track resolution of 1 mrad, while BaBar and PANDA needed only 2.5 mrad resolution.

The pixel and bar size of a DIRC detector are important contributions to the Cherenkov angle resolution for small expansion volumes. The influence of the bar size can, however, be offset by focusing the Cherenkov photons. The FDIRC R&D program first developed the concept of using focusing mirrors for DIRC detectors. The PANDA Barrel DIRC group settled on using a focusing lens between the radiator bar and the expansion volume. A standard lens made of fused silica with an air gap between the lens and the expansion volume was first studied. However, the focal plane of a single lens is highly parabolic in shape. Figure 4.3 shows that while an air gap lens provides good focusing of the Cherenkov pattern in the central region of the ring, where photons are more or less perpendicular to the lens, it becomes defocused nearer to the edges of the pattern and loses photons. This deterioration of the image quality for steeper angles is a combination of lens aberrations, the curved focal plane, and the so-called kaleidoscopic effect [21].

A 2-layer compound lens composed of fused silica and a layer of high-refractive index material Lanthanum crown glass (NLaK33) [22], $n \approx 1.75$, was also studied. This design

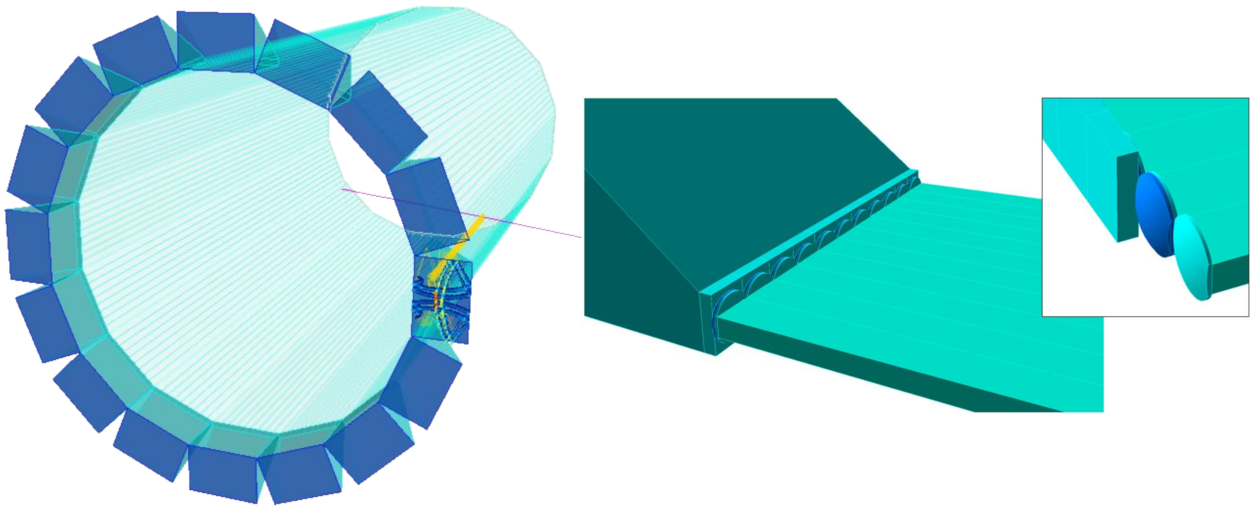

FIG. 4.2: Left: full Geant4 simulation of the current DIRC at EIC baseline design with 16 bar boxes, 176 radiator bars, a 3-layer lens focusing optic, and a 38° prism expansion volume. Right: a zoom in on a single bar box and the layering of the lens.

couples directly to the expansion volume, greatly reducing the loss of photons at steeper angles. Figure 4.4 shows a comparison of the photon yield from a bar radiator with no focusing (green), a standard air gap lens (red), and a 2-layer lens (blue) for two cases. In the 125° case (left) both lenses have comparable photon yields, because the angle between the photons and the lens is fairly shallow. In the 90° case (right), however, the photon yield for the air gap lens is dramatically lowered due to the steep angles between the photons and the lens. The photon yield for the no focusing option is quite deceiving in that it produces a much higher average photon yield than either lens, but the reconstruction of the Cherenkov angle is nearly impossible to within a reasonable measure for the perpendicular case.

The 2-layer lens design solves the problem of photon yield loss from the air gap lens at steeper angles and will allow the PANDA Barrel DIRC to reach their desired separation power. However, as discussed earlier, this separation power of 3 s.d. at 4 GeV/c is unacceptable for the requirements of a DIRC at EIC. The key to solving this problem was in designing a special 3-layer spherical compound lens. The advantage of this 3-layer lens design over a traditional optical lens or the 2-layer lens is the shape of the focal plane. According to simulation the focal plane of the 3-layer lens is relatively flat, as shown in Figure 4.5. Photos of a prototype lens tested at CERN in 2015 and an exploded view of the lens layers and dimensions are shown in Figure 4.6. It contains a layer of NLaK33 sandwiched between two

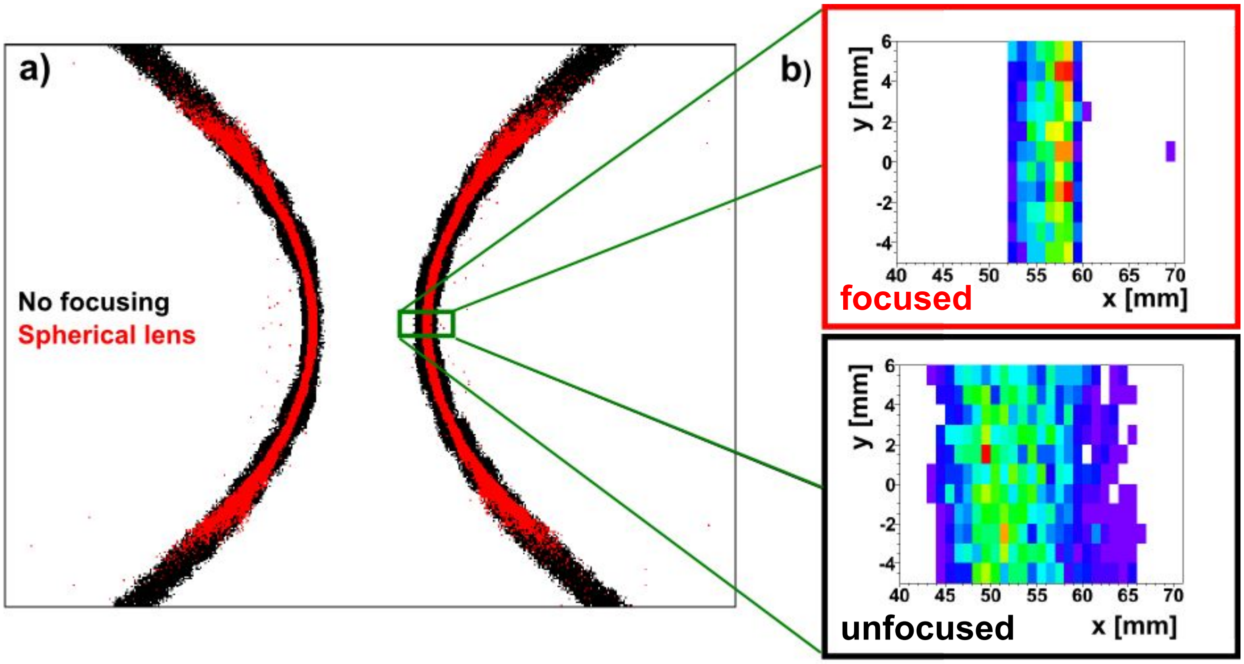

FIG. 4.3: Simulated hit pattern of PANDA DIRC without (black) and with (red) air gap lens focusing (a). On the outer edges of the ring image the lens is becoming dispersive and losing photons, while near the center of the rings the lens does a good job of focusing the image, as seen more clearly in b).

layers of fused silica. The two radii of the middle layer were optimized to remove aberrations present in standard lenses by first defocusing and then refocusing transmitted photons to create a flat focal plane, matching the geometry of the prism expansion volume. Five prototype lenses were produced for evaluating the performance of the lens design in a test beam, for measuring the radiation hardness of the NLaK33 material, and for evaluating the focal plane.

4.1.2 SENSORS

4.2 SIMULATED PERFORMANCE

4.3 POTENTIAL OPTIMIZATIONS

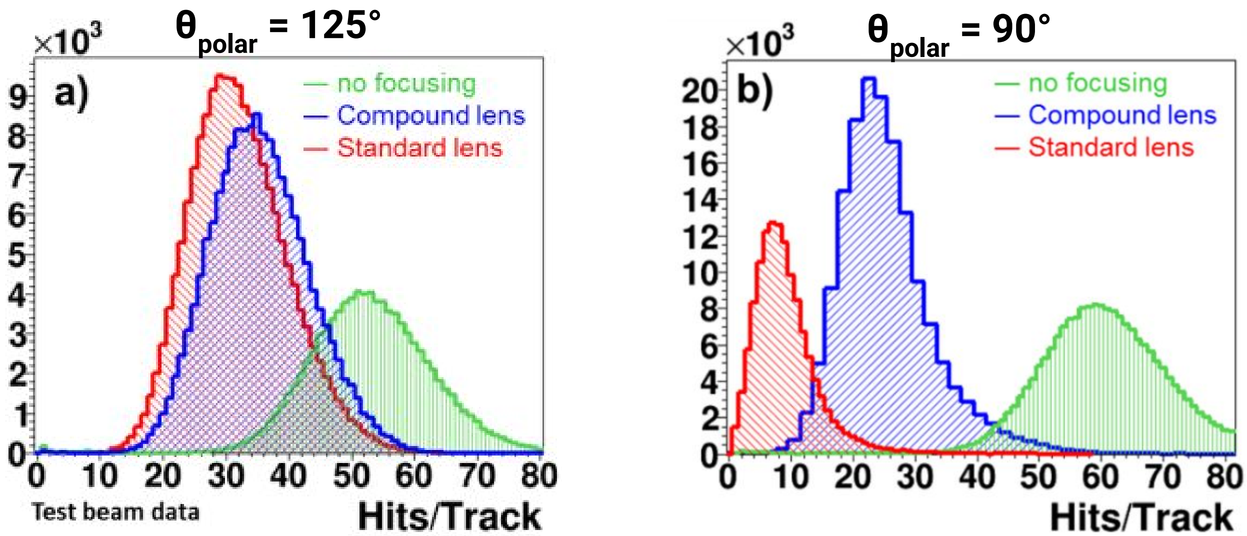

FIG. 4.4: Comparison of the photon yield per track for a DIRC bar with no focusing (green), a standard air gap lens (red), and a 2-layer compound lens (blue) for polar angles of 125° (left) and 90° (right). The standard and compound lenses have comparable yields at 125°, but the standard lens clearly loses a large amount of photons in the perpendicular case.

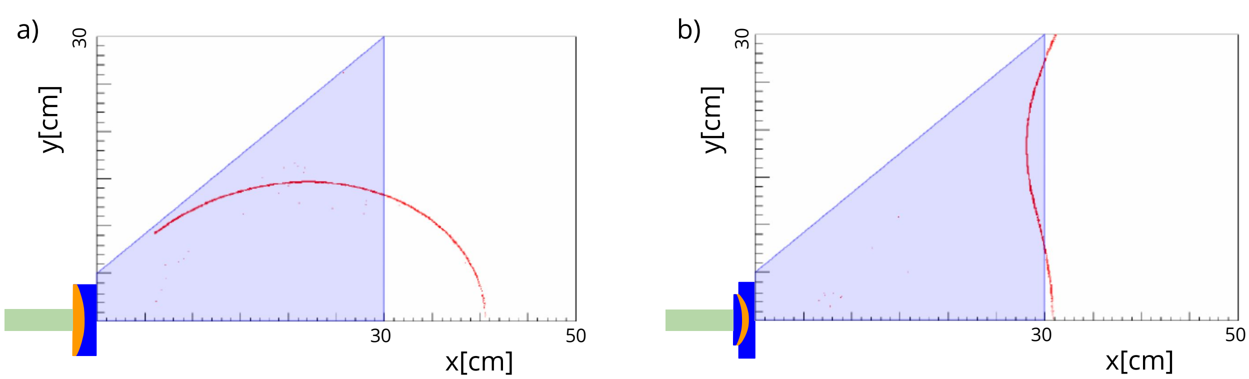

FIG. 4.5: The simulated focal planes (red lines) of a 2-layer lens (left) and the 3-layer lens (right) compared to the shape of the expansion volume prism (grey). Obviously the focal plane of the 2-layer lens is highly parabolic in shape, whereas the 3-layer lens focal plane is relatively flat, allowing for a better resolution of the Cherenkov angle.

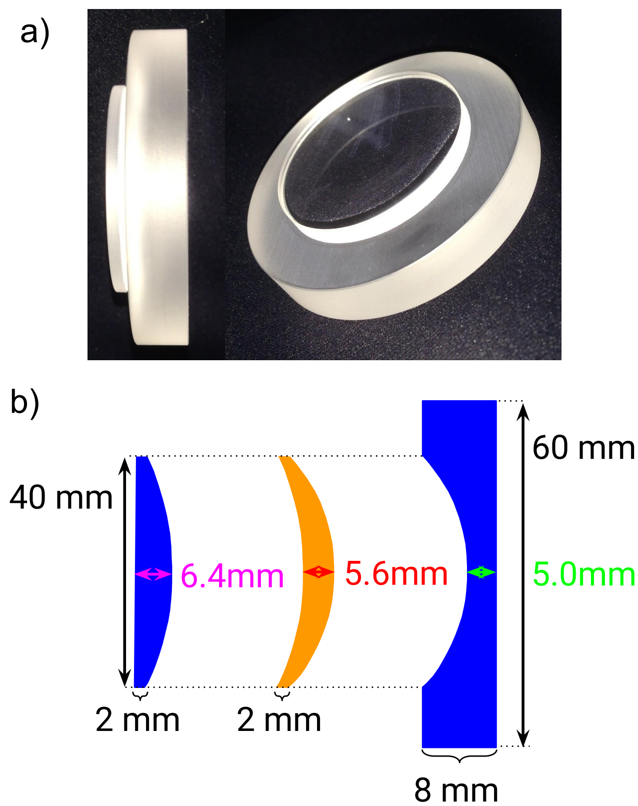

FIG. 4.6: Prototype 3-layer lens built for optical testing (a), and an exploded view of each layer with dimensions (b).

CHAPTER 5

TESTING DIRC COMPONENTS

The validation of the key components of the DIRC for an EIC discussed in Chapter 4 is vital to show that the Geant4 simulation package produces results expected for the real detector. However, due to budget restraints it was not possible to build or otherwise procure a full scale prototype of the envisioned EIC DIRC discussed in Chapter 4 (e.g. 2×2 mm^2 pixel MCP-PMTs are not currently available commercially). Instead a series of test bench measurements have been made to validate simulated performance of the new 3-layer lens design, study the radiation hardness of the NLaK33 material, and evaluate the performance of MCP-PMTs in high magnetic field environments.

5.1 OPTICAL PROPERTIES OF 3-LAYER LENS

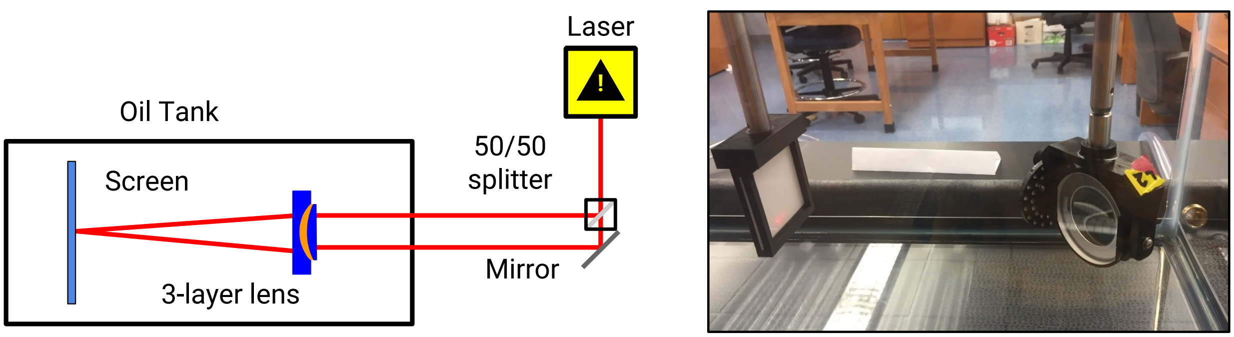

FIG. 5.1: Schematic drawing of the setup built at Old Dominion University for testing the optical properties of the 3-layer lens design (left), and a closeup view of the lens and screen inside the actual setup (right).

To measure the shape of the focal plane a setup was designed and built at Old Dominion University, shown in Figure 5.1, in which a laser shines through a 50/50 beam splitter and a mirror to make two beams that are parallel to within 0.5 degrees across roughly 10 meters. The beams then pass through a $30 \times 40 \times 60$ cm^3 glass container filled with mineral oil with a refractive index similar to that of fused silica to simulate the behavior of light passing from bar to lens to expansion volume. The beams are focused through the 3-layer lens, being held in a specially designed holder that allows the lens to be rotated in two planes (Figure 5.2).

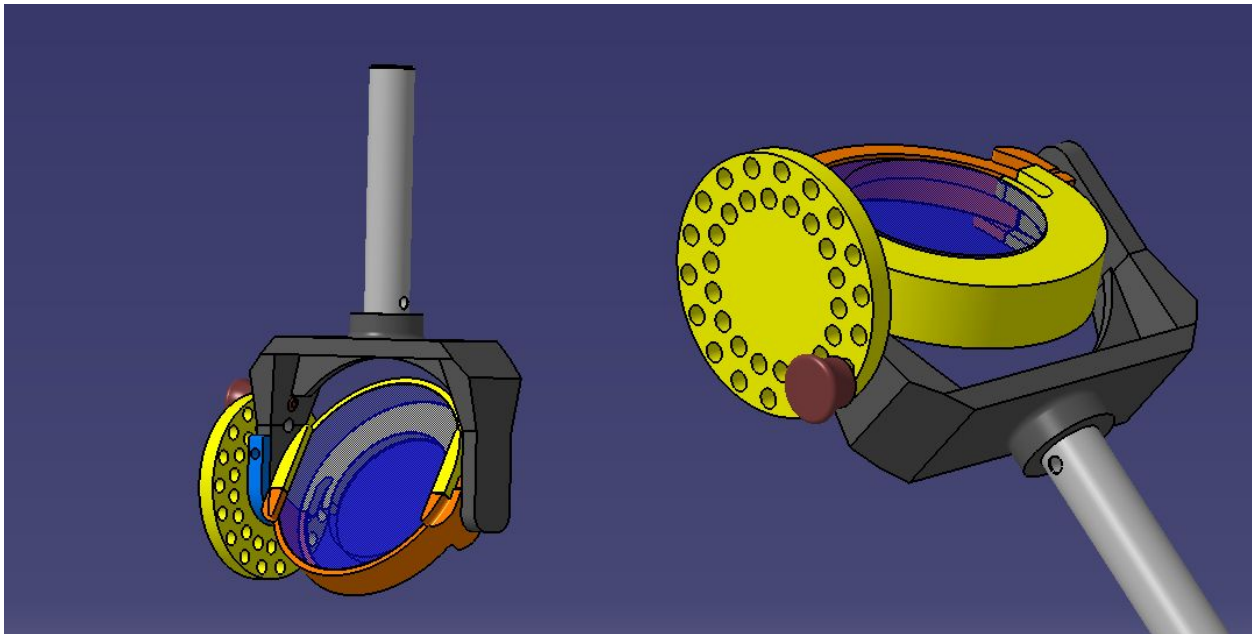

FIG. 5.2: CAD drawing of 3-layer lens holder which lets the lens rotate in two planes, allowing the full 3D focal plane to be mapped.

Finally the beams are focused onto a plastic screen inside the tank and intersection of the two beams determines the focal length.

Measurements were initially taken with a 632 nm red helium-neon laser, but the beam spot was too large and very distorted. A 530 nm wavelength green laser with a 1 mm beam spot was then purchased to replace the red laser. Initial results with a 5 mm beam separation are shown in Figure 5.3. Obviously there is a large discrepancy in both position and shape of the measured and simulated focal plane. This was rectified by discovering that in the simulation it was assumed that the two beams were entering the lens at fixed points on the lens' face regardless of lens rotation, where as in the experiment the rotation of the lens about it's center causes the beams to shift with respect to the lens face. When rotating at the edge of the lens closest to the laser rather than through the center this difference is negligible, as illustrated in Figure 5.4.

A correction was implemented in the Geant4 simulation to account for the shift of the beam spot during rotation, the results of which can be seen in Figure 5.5a. The beams have since been brought to a 2 mm separation to reduce effects of aberration and a second lens holder was 3D printed to allow for rotation about the edge of the lens. A new round of data was taken and results are shown in Figure 5.5b. This change vastly improved the results

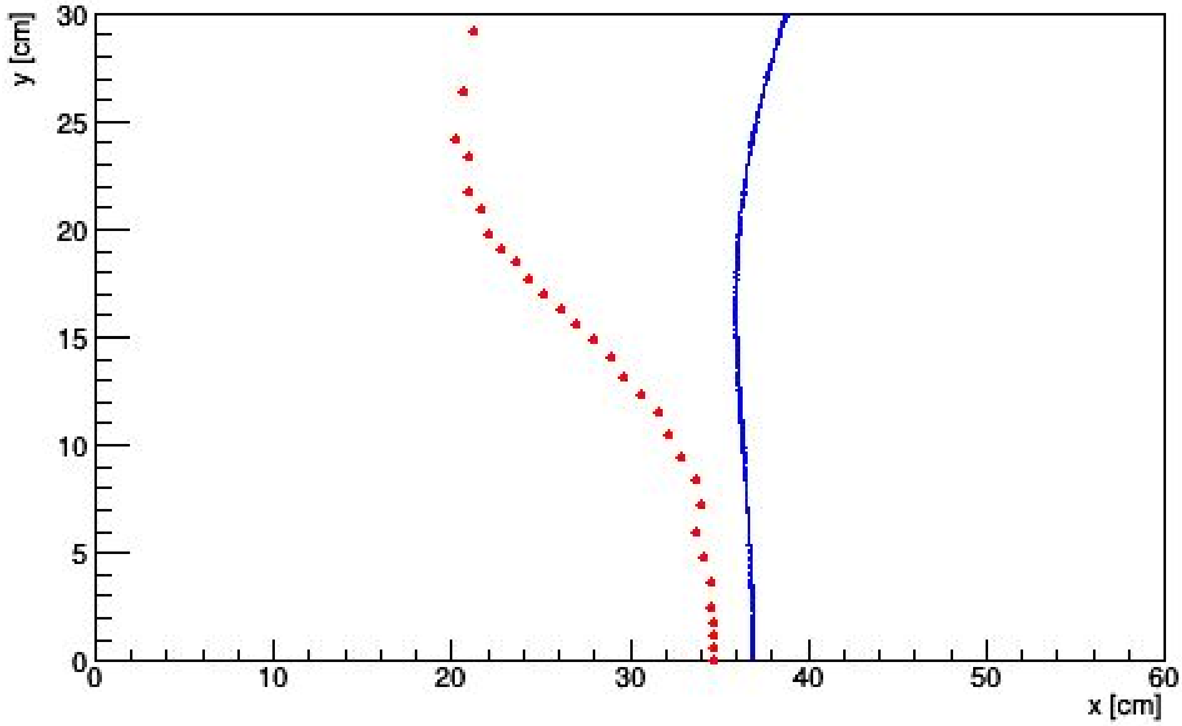

FIG. 5.3: Initial measurement of the 3-layer lens focal plane using the upgraded green laser (red dots) compared to simulation (blue line).

of both the simulation from the first measurement and the results of the second, showing that the simulation indeed reproduces very nicely the shape of the focal plane, although the position is still roughly 3 cm too long. This could be explained by reducing the radius of the second layer of the lens by 2 mm, but as of this writing there is no reliable way of measuring the radius to such a degree.

5.2 RADIATION HARDNESS OF NLAK33

Fused silica, which is used for most of the optical components in all current DIRC designs, was already extensively tested in the BaBar and PANDA experiments and proved to be radiation hard. The determination of the radiation hardness of NLaK33 is an important study for the EIC R&D program. The irradiation of both a pure sample of NLaK33 and a prototype lens was performed at Catholic University of America in a setup with 160 keV X-rays (Figure 5.6a) in 20 steps, with each step delivering a dose of 0.5 krad. Between each step the transmission properties of both the pure sample and the prototype lens were

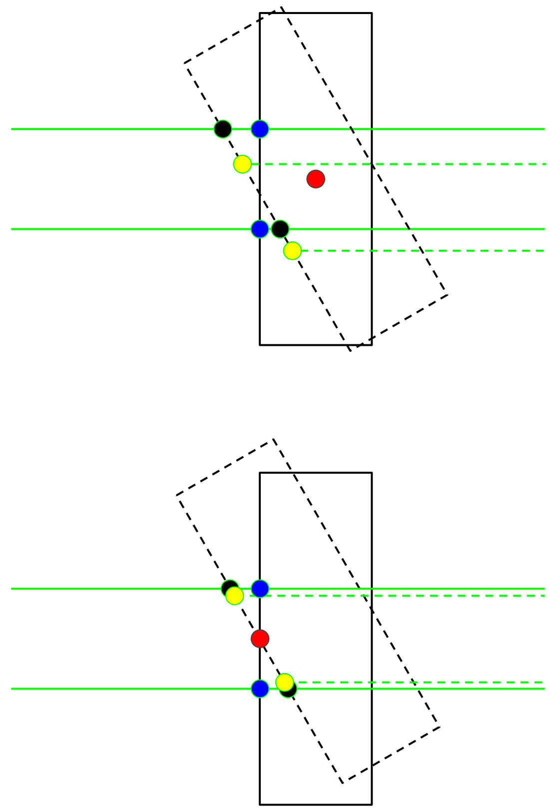

FIG. 5.4: Schematic of the discrepancy between beam positions in data (black) and simulation (yellow) in relation to the original beam positions (blue) for a given rotation point (red) at the center (top) of the lens, or at the edge (bottom) of the lens.

measured with a monochromator (Figure 5.6b) with a reproducibility of 0.2% to quantify the radiation impact.

5.3 PERFORMANCE OF MCP-PMTS IN HIGH MAGNETIC FIELD

Due to the limiting space requirements of the EIC DIRC design, as mentioned in Chapter 4, this places a unique set of requirements on the DIRC readout sensors. In order to achieve the desired single photon resolution while maintaining a sufficiently sized expansion volume the sensors, and therefore the pixels, must be small. Furthermore, due to the positioning of the readout plane being inside the large field of the solenoid magnet (see Figure 2.5) these sensors must also have a high tolerance to magnetic fields, both in magnitude (up to 3 T or higher), non-uniformity, and orientation. It was with these requirements in mind that the use of Micro-channel plate photomultiplier tubes (MCP-PMTs) was proposed (Figure 5.7). MCP-PMTs have a much higher resistance to external magnetic fields than traditional photomultipliers, with studies being done up to 2 T [23], [24], [25], [26], [27], [28]. The tests described below are the first to study the effects of fields as large as 5 T on MCP-PMTs.

In the fall of 2014 and summers of 2015 and 2016 several different MCP-PMTs were tested at Jefferson Lab [6]. The FROST superconducting solenoidal magnet with a field tunable up to 5 T with a cylindrical bore diameter of 12.7 cm and a length of 76.2 cm was used for testing [29]. The central field of the magnet, while quite large, is also very homogeneous, with an inhomogeneity of less than 5×10^{-5} over a cylindrical volume with a diameter of 1.5 cm and a length of 5 cm. The sensors that were tested were held in place at the center of the magnet using a custom-built, non-magnetic, light-tight cylindrical dark box, as shown in Figure 5.8. Inside the dark box the sensor was held in place by a turn table that allowed for rotation around a vertical axis as well as a horizontal axis (the Y(Y') and Z(Z') axes in Figure 5.9 respectively). The range of the polar angle θ was dependent on the size of the sensor being measured and the signal- and high-voltage cables connected to the back of the sensor. A cart allowed the sensor to move relative to the dark box for precise position and the center of the magnet.

A pulser-driven LED was used to illuminate the MCP-PMTs with 470 nm photons. An optical fiber was used to transmit the photons to the dark box and a diffuser installed inside the dark box cap was used to illuminate the entire face of the sensor with nearly constant intensity and 10 ns wide pulses at 30 kHz. The sensor signal output was then amplified using a 200-times preamplifier and used as input to a flash analog-to-digital converter (fADC). The fADC was then read out by our data acquisition system (DAQ).The pulser was also used as the trigger signal for the fADC, as shown in the chart in Figure 5.9 (right).

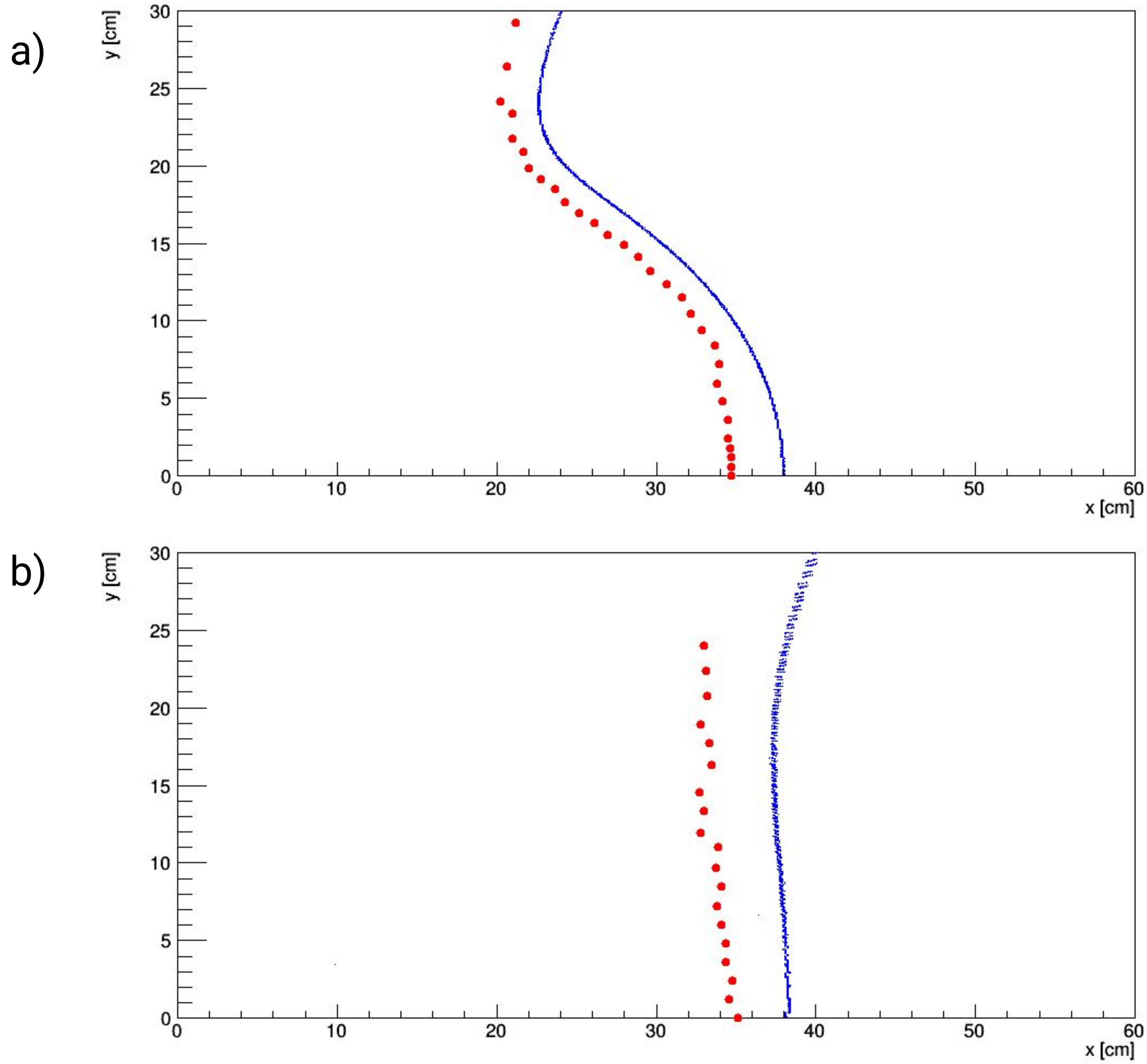

FIG. 5.5: Initial measurement of the 3-layer lens focal plane compared to a rotation corrected simulation (a), and a second measurement with a tighter (2 mm) beam configuration and a modified lens holder (b).

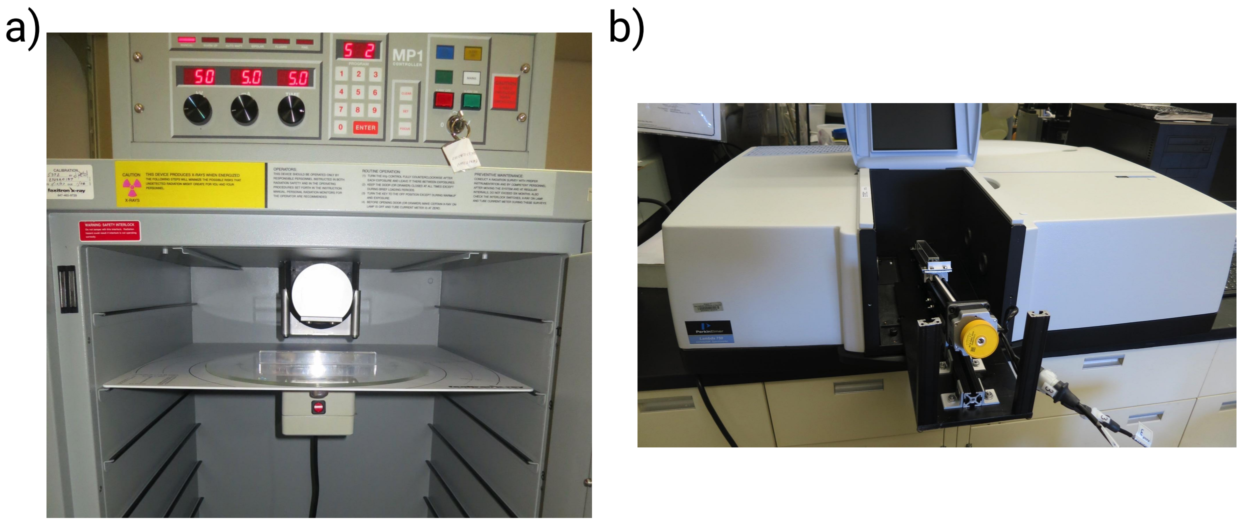

FIG. 5.6: X-ray source (a) and monochromator (b) used for testing the radiation hardness through transmission degradation of NLaK33 samples at Catholic University of America.

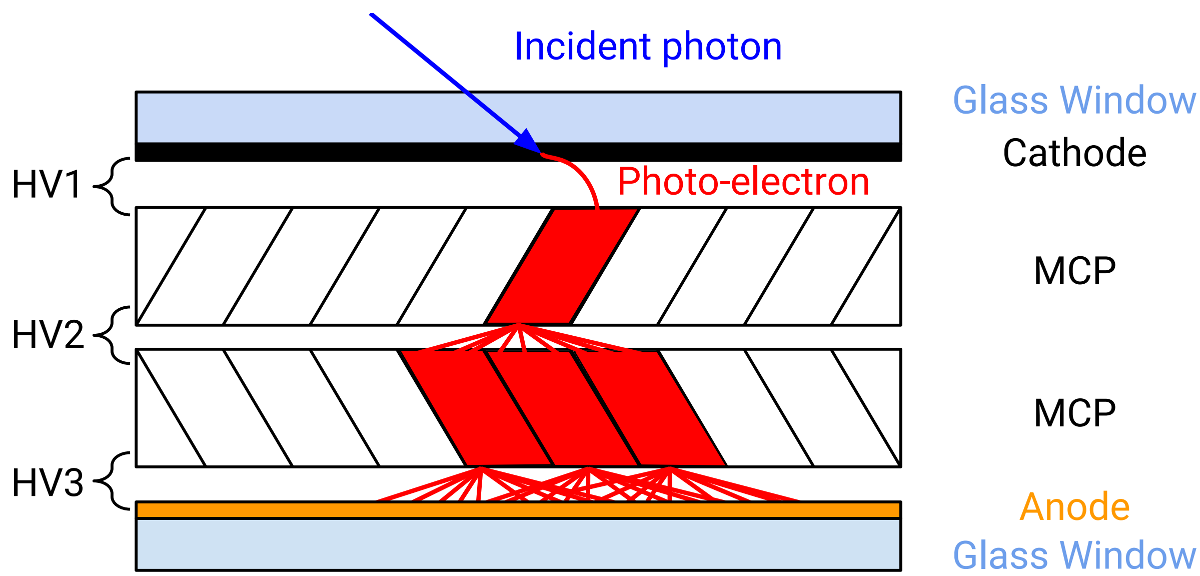

FIG. 5.7: Schematic of the Micro-channel Plate photo-multiplier tube (MCP-PMT) concept. A cathode and anode sandwich two conducting plates with micrometer-sized channels (MCP) in a chevron pattern. An incident photon (blue) strikes the cathode, producing a photo-electron (red). That electron is accelerated through the potential difference between the cathode and first MCP (HV1) before striking the inside of one channel. This creates the same effect as an electron striking the dynode of a typical PMT, resulting in an avalanche of photo-electrons that emerge out of the other side of the first MCP. These electrons are again accelerated through a second potential difference (HV2) before repeating the process in the second MCP. Finally, the copious photo-electrons exit the second MCP, are accelerated through a final potential difference (HV3), and are collected on the anode. This design is both much more compact and much more resistant to magnetic fields compared to traditional PMTs.

FIG. 5.8: The FROST superconducting magnet with the dark box placed in the bore.

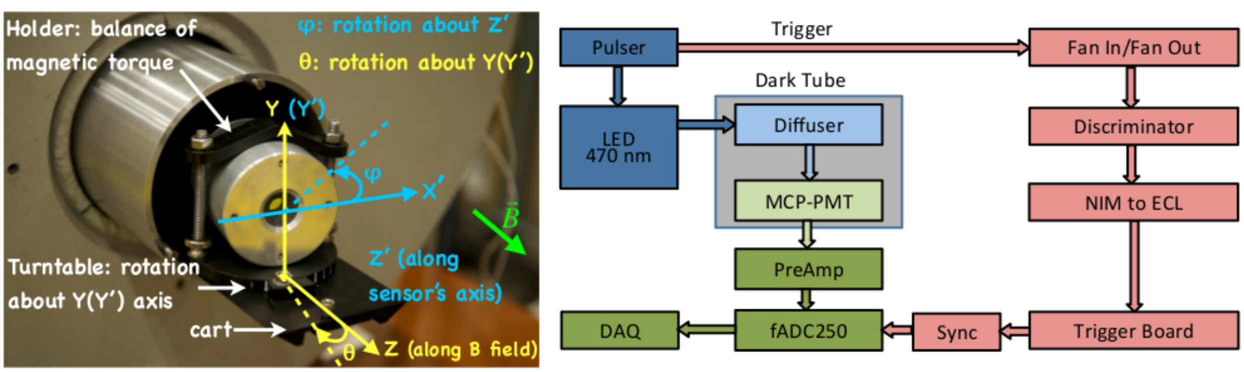

FIG. 5.9: Left: A closeup of the dark box showing the Photek PMT210 being held in place by the turn table. This setup allows the MCP-PMT to be rotated around both the horizontal Z(Z') axis as well as the vertical Y(Y') axis (with respect to the floor). The rotation about the Y(Y') and Z(Z') axes are described by the polar angle θ and azimuthal angle ϕ respectively. The magnetic field is parallel to the central axis of the dark box. Right: A flowchart of the readout used for testing. The photocathode is exposed to single 470 nm photons to produce photoelectrons, with a large voltage difference between the anode and cathode used to create an avalanche. The total charge is collected on the anode, amplified by a preamplifier, and digitized by an fADC and read out by a DAQ. [6]

CHAPTER 6

3-LAYER LENS PERFORMANCE IN PARTICLE BEAM

6.1 SIMULATED PERFORMANCE

6.2 2015 TEST BEAM PROTOTYPE SETUP

6.3 DATA ANALYSIS

6.3.1 ERROR EVALUATION

CHAPTER 7

OUTLOOK AND SUMMARY

BIBLIOGRAPHY

[1] S. Shimizu. Low Q**2 Structure Functions including the Longitudinal Structure Function. In *QCD and high energy interactions. Proceedings, 44th Rencontres de Moriond, La Thuile, Italy, March 14-21, 2009*, pages 301–304, 2009.

[2] A. Accardi et al. Electron Ion Collider: The Next QCD Frontier - Understanding the glue that binds us all. *Eur. Phys. J.*, A52(9):268, 2016.

[3] S. Malace et al. The Challenge of the EMC Effect: existing data and future directions. *Int. J. Mod. Phys.*, E23(08):1430013, 2014.

[4] S. Agostinelli et al. GEANT4: A Simulation toolkit. *Nucl. Instrum. Meth.*, A506:250–303, 2003.

[5] R. Dzhygadlo et al. The PANDA Barrel DIRC. *JINST*, 11(05):C05013, 2016.

[6] Y. Ilieva et al. MCP-PMT studies at the High-B test facility at Jefferson Lab. *JINST*, 11(03):C03061, 2016.

[7] B. Carithers and P. Grannis. Discovery of the top quark. *Beam Line*, 25(3):4–16, 1995.

[8] R. Tribble et al. *Frontiers of Nuclear Science*. 2007.

[9] L. B. Weinstein et al. Short Range Correlations and the EMC Effect. *Phys. Rev. Lett.*, 106:052301, 2011.

[10] V. Guzey et al. Evidence for nuclear gluon shadowing from the ALICE measurements of PbPb ultraperipheral exclusive J/ψ production. *Phys. Lett.*, B726:290–295, 2013.

[11] S. Abeyratne et al. MEIC Design Summary. 2015.

[12] E. C. Aschenauer et al. eRHIC Design Study: An Electron-Ion Collider at BNL. 2014.

[13] A. A. Watson. The Discovery of Cherenkov Radiation and its use in the detection of extensive air showers. *Nucl. Phys. Proc. Suppl.*, 212-213:13–19, 2011.

[14] C. Grupen and I. Buvat, editors. *Handbook of particle detection and imaging, vol. 1 and vol.2*. Springer, Berlin, Germany, 2012.

[15] J. Schwiening. Construction and Performance of the BaBar DIRC. *JINST*, 4:P10004, 2009.

[16] J. Va'vra et al. The Focusing DIRC - the First RICH Detector to Correct the Chromatic Error by Timing, and the Development of a New TOF Detector Concept. In *Instrumentation. Proceedings, 11th International Conference, VCI 11, Vienna, Austria, February 19-24, 2007*, 2007. [Submitted to: Nucl. Instrum. Meth.(2007)].

[17] E. Etzelmller et al. Tests and developments of the PANDA Endcap Disc DIRC. *JINST*, 11(04):C04014, 2016.

[18] E. Torassa. Particle identification with the TOP and ARICH detectors at Belle II. *Nucl. Instrum. Meth.*, A824:152–155, 2016.

[19] K. Fhl et al. TORCH - Cherenkov and Time-of-Flight PID Detector for the LHCb Upgrade at CERN. *JINST*, 11(05):C05020, 2016.

[20] J. Stevens et al. The GlueX DIRC Project. *JINST*, 11(07):C07010, 2016.

[21] J. Va'vra. Simulation of the Focusing DIRC Optics with Mathematica. In *Proceedings, 2008 IEEE Nuclear Science Symposium, Medical Imaging Conference and 16th International Workshop on Room-Temperature Semiconductor X-Ray and Gamma-Ray Detectors (NSS/MIC 2008 / RTSD 2008): Dresden, Germany, October 19-25, 2008*, pages 2408–2412, 2008.

[22] SCHOTT North America. *Optical Glass Data Sheets*, 6 2015.

[23] F. Uhlig et al. Performance studies of microchannel plate PMTs. *Nucl. Instrum. Meth.*, A695:68–70, 2012.

[24] A. Lehmann et al. Systematic studies of micro-channel plate PMTs. *Nucl. Instrum. Meth.*, A639:144–147, 2011.

[25] A. Lehmann et al. Performance studies of microchannel plate PMTs in high magnetic fields. *Nucl. Instrum. Meth.*, A595:173–176, 2008.

[26] S. Hirose. Performance of the MCP-PMT for the Belle II TOP counter in a magnetic field. *Nucl. Instrum. Meth.*, A766:163–166, 2014.

[27] M. Akatsu et al. MCP-PMT timing property for single photons. *Nucl. Instrum. Meth.*, A528:763–775, 2004.

[28] S. Korpar et al. Photonis MCP PMT as a light sensor for the Belle II RICH. *Nucl. Instrum. Meth.*, A639:162–164, 2011.

[29] C. D. Keith et al. The Jefferson Lab Frozen Spin Target. *Nucl. Instrum. Meth.*, A684:27–35, 2012.

APPENDIX A

ERROR EVALUATION

VITA

S. Lee Allison
Department of Physics
Old Dominion University
Norfolk, VA 23529

The text of the Vita goes here.

Typeset using LaTeX.